INL/RPT-24-79849-Revision-0

Defect Production and Microstructural Feature Impact for Radiation Damage in Additively Manufactured 316 Stainless Steel

August 2024

Andrea M Jokisaari, Sourabh Bhagwan Kadambi, Sanjoy Kumar Mazumder, Mathew M Swisher, William T Yorgason

Changing the World's Energy Future

Idaho National Laboratory

INL is a U.S. Department of Energy National Laboratory operated by Battelle Energy Alliance, LLC

INL/RPT-24-79849-Revision-0

Defect Production and Microstructural Feature Impact for Radiation Damage in Additively Manufactured 316 Stainless Steel

Andrea M Jokisaari, Sourabh Bhagwan Kadambi, Sanjoy Kumar Mazumder, Mathew M Swisher, William T Yorgason

August 2024

Idaho National Laboratory
Idaho Falls, Idaho 83415

http://www.inl.gov

Prepared for the
U.S. Department of Energy
Under DOE Idaho Operations Office
Contract DE-AC07-05ID14517

INL/RPT-24-79849

Advanced Materials and Manufacturing Technologies

Defect Production And Microstructural Feature Impact For Radiation Damage In Additively Manufactured 316 Stainless Steel

JULY 2024

Andrea M. Jokisaari, Sourabh Bhagwan Kadambi, Sanjoy K. Mazumder, Mathew Swisher, and W. Tanner Yorgason

Idaho National Laboratory

Idaho National Laboratory

Battelle Energy Alliance manages INL for the U.S. Department of Energy's Office of Nuclear Energy

INL/RPT-24-79849

Defect Production And Microstructural Feature Impact For Radiation Damage In Additively Manufactured 316 Stainless Steel

**Andrea M. Jokisaari, Sourabh Bhagwan Kadambi,
Sanjoy K. Mazumder, Mathew Swisher, and
W. Tanner Yorgason
Idaho National Laboratory**

July 2024

**Idaho National Laboratory
Idaho Falls, Idaho 83415**

http://www.inl.gov

**Prepared for the
U.S. Department of Energy
Office of Nuclear Energy
Under DOE Idaho Operations Office
Contract DE-AC07-05ID14517**

Page intentionally left blank

ABSTRACT

This milestone presents multi-scale modeling research results for additively manufactured 316 stainless steel. A combination of phase field, cluster dynamics, molecular dynamics, and density functional theory with machine learning is used, allowing for predictions of radiation-driven microstructural evolution in additively manufactured 316 stainless steel over a range of temperatures, damage rates, neutron spectra, and microstructures. This effort is integral to the development of combined ion and neutron irradiation testing for material qualification. Informed by ion irradiation and neutron irradiation results across the Department of Energy Office of Nuclear Energy's Advanced Materials and Manufacturing Technologies program, we investigate the unique aspects of radiation-driven microstructure evolution in additively manufactured 316 stainless steel. In particular, we focus on understanding the impact of carbon concentration (varying, for example, between the 316L and 316H standards) on void formation; radiation-induced segregation at dislocation cells and grain boundaries; and the evolution of dislocation loops and network dislocation populations with damage rate and temperature. We find that the unique characteristics of the additively manufactured microstructures must be accounted for in understanding the evolution of dislocation and void populations under thermal and irradiation conditions, such as the variation in sink strengths arising due to the variation in dislocation density. We also find that the radiation-induced segregation of Cr and Ni to grain boundaries and cell walls differs due to the differences in their defect sink biases. In addition, we find that increasing the Ni content can slow vacancy diffusion, which may provide a mechanism for the observed reduction in transient swelling rate for austenitic Fe-Cr-Ni alloys with increasing Ni content. Furthermore, ion irradiations have shown that increasing carbon content in 316 SS results in a larger population of smaller voids, suggesting reduced vacancy diffusion. Our results support the hypothesis developed from the ion irradiation results, showing that the carbon content of additively manufactured 316 SS has a significant impact on the migration rate of defect clusters. The presence of carbon atoms results in carbon-vacancy trapping, significantly reducing the diffusion rate of vacancies. Carbon atoms may also be trapped near the surface of a void, which may reduce void growth by trapping vacancies that diffuse toward the void.

Page intentionally left blank

ACKNOWLEDGMENTS

This work was funded by the Advanced Materials and Manufacturing Technologies program, which is supported by the Office of Nuclear Energy of the U.S. Department of Energy. This research made use of the resources of the High Performance Computing Center at Idaho National Laboratory, which is supported by the Office of Nuclear Energy of the U.S. Department of Energy and the Nuclear Science User Facilities under Contract No. DE-AC07-05ID14517.

Page intentionally left blank

CONTENTS

FIGURES

TABLES

Page intentionally left blank

ACRONYMS

0D	zero-dimensional
2D	two-dimensional
AM	additively manufactured
AMMT	Advanced Materials and Manufacturing Technologies
BCC	body-centered cubic
CD	cluster dynamics
DFT	density functional theory
dpa	displacements per atom
EAM	embedded atom method
FCC	face-centered cubic
GBs	grain boundaries
GPR	Gaussian process regression
KMC	kinetic Monte Carlo
LAMMPS	Large scale Atomistic/Molecular Massively Parallel Simulator
LPBF	laser powder bed fusion
MD	molecular dynamics
MGPR	modified Gaussian process regression
ML-NEB	machine-learned nudged elastic band
MOOSE	Multiphysics Object-Oriented Simulation Environment
NEB	nudged elastic band
NN	nearest neighbors
PES	potential energy surface

RIS radiation-induced segregation

SDP size distribution plot

SIA self-interstitial atom

SS stainless steel

VASP Vienna Ab-initio Simulation Package

Page intentionally left blank

Defect Production and Microstructural Feature Impact for Radiation Damage in Additively Manufactured 316 Stainless Steel

1. INTRODUCTION

Metal additive manufacturing provides an opportunity to deploy novel materials and component geometries in nuclear reactors, which may improve overall performance and reduce costs. Deployment of additively manufactured (AM) materials and components into nuclear reactors requires a quantitative prediction of the material ability to withstand the irradiation environment. Due to both the significant degree of resulting microstructure variability intrinsic to additive manufacturing as well as the limited throughput possible in materials test reactors, it is impractical to rely solely on neutron irradiation to provide qualification data. Therefore, modeling must be leveraged to fill the gaps.

The Advanced Materials and Manufacturing Technologies (AMMT) program under the Department of Energy Office of Nuclear Energy is focusing on laser powder bed fusion (LPBF) 316 stainless steel (SS) to demonstrate its new accelerated development and qualification methods. Thus, modeling efforts on radiation effects are focused on this material to understand the impact of microstructure and microchemical variability on radiation-driven microstructure evolution. As-manufactured LPBF 316 has a complex multiscale structure including high angle grain boundariess (GBss) with chemical segregation and dislocation cells within grains that also exhibit chemical micro-segregation. Informed by ion irradiation and neutron irradiation results across the AMMT program, we focus on developing physics-based and machine learning models for the unique aspects of radiation damage in LPBF 316. In particular, we focus on understanding the impact of carbon concentration (varying, for example, between the 316L and 316H standards) on void formation; radiation-induced segregation at dislocation cells and grain boundaries; and the evolution of dislocation loops and network dislocation populations. We use a combination of phase field, cluster dynamics, molecular dynamics,

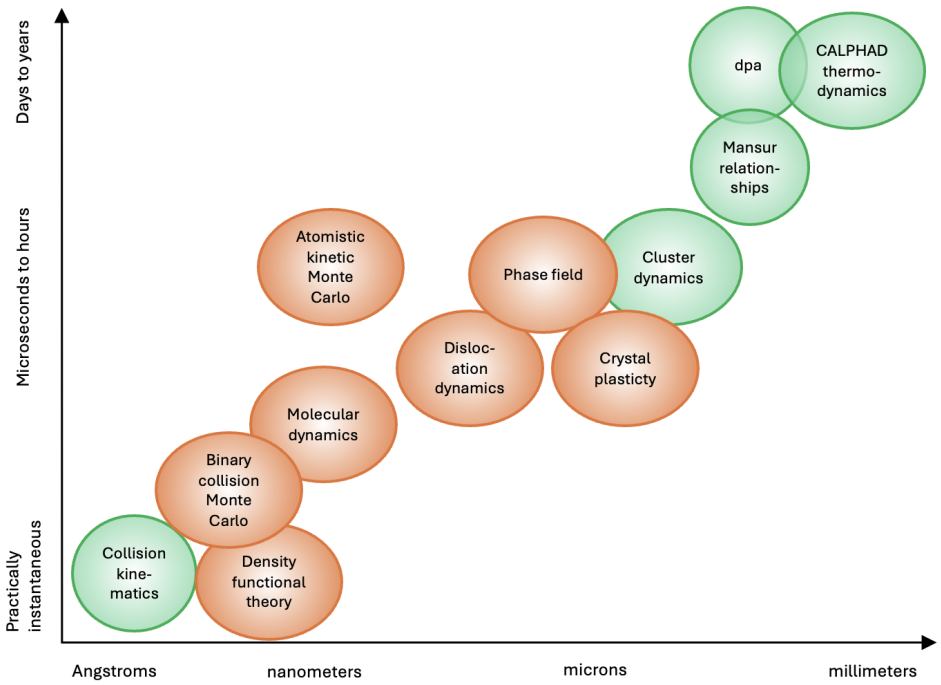

Figure 1. The physical modeling and theories used to assess radiation-affected phenomena. Green denotes mean-field methods and orange denotes spatially-resolved methods (note that some methods can in fact be used in both ways).

and density functional theory with machine learning (Fig. 1. This combined modeling approach allows for predictions of radiation-driven microstructural evolution in LPBF 316 SS over a range of temperatures, displacements per atom (dpa) damage rates, neutron spectra, and microstructures and is integral to the effort to use combined ion and neutron irradiation testing for material qualification.

2. SPATIALLY-RESOLVED MICROSTRUCTURE MODELING

Compared to conventionally cast or wrought 316 SS, AM 316 SS alloys are expected to show a distinct response to irradiation damage owing to their as-printed dislocation cell structure. In this work, we develop a modeling capability that enables quantitative simulation of spatially-resolved microstructure evolution in AM 316 SS. To this end, we model the evolution of network dislocations within cells and cell walls of the AM microstructure by means of climb-mediated mechanisms. Rate-theory equations are employed to describe the evolution of non-equilibrium point defect concentrations that simultaneously result in dislocation line

generation and dipole annihilation. The spatially-resolved dislocation evolution model is coupled with a radiation-induced segregation (RIS) model we developed in fiscal year 2023 [1] to simulate composition changes at dislocation cell walls and GBs. The model is parameterized for face-centered cubic (FCC) Fe-Cr-Ni as a representative system for 316 SS.

2.1. Model Formulation

In this section, we first introduce the RIS model and the sink strength of edge dislocations. We then present the models for dislocation climb-mediated evolution under thermal and irradiation conditions.

2.1.1. Radiation-Induced Segregation

The evolution equations for RIS are given in the diffusion form following our derivation in Ref. [1] as

$$\frac{\partial c_{Ni}}{\partial t} = \boldsymbol{\nabla}.\left(\tilde{D}_{NiNi}\boldsymbol{\nabla}c_{Ni} + \tilde{D}_{NiCr}\boldsymbol{\nabla}c_{Cr} + D_{NiV}\boldsymbol{\nabla}c_V + D_{NiI}\boldsymbol{\nabla}c_I\right), \tag{1a}$$

$$\frac{\partial c_{Cr}}{\partial t} = -\boldsymbol{\nabla}.\left(\tilde{D}_{CrNi}\boldsymbol{\nabla}c_{Ni} + \tilde{D}_{CrCr}\boldsymbol{\nabla}c_{Cr} + D_{CrV}\boldsymbol{\nabla}c_V + D_{CrI}\boldsymbol{\nabla}c_I\right), \tag{1b}$$

$$\frac{\partial\, c_V}{\partial t} = -\boldsymbol{\nabla}.\left(\tilde{D}_{VNi}\boldsymbol{\nabla}c_{Ni} + \tilde{D}_{VCr}\boldsymbol{\nabla}c_{Cr} + D_V\boldsymbol{\nabla}c_V\right) + \dot{P}_V - \rho Z_V D_V(c_V - c_V^e) - \dot{R}_{VI}c_V c_I, \tag{1c}$$

$$\frac{\partial\, c_I}{\partial t} = -\boldsymbol{\nabla}.\left(\tilde{D}_{INi}\boldsymbol{\nabla}c_{Ni} + \tilde{D}_{ICr}\boldsymbol{\nabla}c_{Cr} + D_I\boldsymbol{\nabla}c_I\right) + \dot{P}_I - \rho Z_I D_I c_I - \dot{R}_{VI}c_V c_I. \tag{1d}$$

Here, $\dot{P}_\nu$ is the point defect production rate, with ν denoting vacancy (V) or self-interstitial atom (SIA, I). $\dot{R}_{VI} = 4\pi r_\circ(D_V + D_I)/V_a$ is the vacancy-self-interstitial atom (SIA) recombination rate with $r_\circ$ being the recombination radius. Z is the non-dimensional sink strength or efficiency for edge dislocations. The point defects are absorbed by dislocations with a sink strength given by $k_\nu^2 = \rho Z_\nu$, where ρ is the line dislocation density. We define the concentrations as lattice site fractions, c, in the lattice frame of reference and choose Fe as the dependent species. Note that the equation for the evolution of the iron atomic fraction, c_{Fe}, is implicitly described by $c_{Fe} = 1 - c_{Ni} - c_{Cr} - c_v + c_i$.

Faster diffusion through the dislocation network is incorporated by describing an effective partial diffusivity as $d = d_{\text{bulk}} + \rho b^2 d_{\text{pipe}}$, where d_{bulk} is the bulk diffusivity and d_{pipe} is the pipe diffusivity

given by a barrier energy that is assumed to one-third of the bulk [2].

2.1.2. Dislocation Network Evolution

The evolution of the dislocation density at any point in the system is described as the sum of line incorporation (i) due to a Bardeen-Herring source [3] and annihilation (a) of edge dipoles due to climb [4] as

$$\frac{d\rho}{dt} = \left.\frac{d\rho}{dt}\right|_i + \left.\frac{d\rho}{dt}\right|_a, \tag{2a}$$

$$\left.\frac{d\rho}{dt}\right|_i = \frac{\rho v_{\text{cl}}}{l_{\text{mesh}}}, \tag{2b}$$

$$\left.\frac{d\rho}{dt}\right|_a = -c_{\text{cl},2}\frac{\rho}{\tau_{\text{cl}}}. \tag{2c}$$

where l_{mesh} is a characteristic length in the model of Ref. [3]. v_{cl} is the dislocation climb velocity, which we model as

$$v_{\text{cl}} = \frac{1}{b}\left[(Z_I + \zeta_I)D_I c_I - (Z_V + \zeta_V)D_V(c_V - c_V^{d,e})\right], \tag{3}$$

where we defined $\zeta_\nu = \alpha\sigma_\nu^d$ as the deviation in Z_ν due to the distribution in the dislocation spacing/density. σ_ν^d is the standard deviation and $\alpha = 3$ is assumed. Based on Ref. [3], a similar form of the expression can be written as

$$v_{\text{cl}} = \frac{1}{b}\left[(Z_I(1 + \alpha\zeta_\circ)D_I c_I - Z_V D_V(c_V - c_V^{d,e})\right], \tag{4}$$

where $\zeta_\circ = 0.5\left[1 - \exp\left(-\lambda\rho\right)\right]$. In Ref. [3], $\lambda = 10^3$ nm^2 was set such that the normalized deviation $\alpha\zeta_\circ$ becomes negligible for $\rho \leq 10^{-3}$ nm^{-2} and achieves a maximum at $\rho \approx 10^{-2}$ nm^{-2}. With c_V^e being the thermal equilibrium concentration of the vacancy in the bulk, the equilibrium concentration near a dislocation

$c_V^{d,e}$ arising from the stress field of the other dislocation in the dipole is given by

$$c_V^{d,e} = c_V^e \exp\left(\frac{Hb}{h}\right), \tag{5a}$$

$$H = \frac{GV_\mathrm{a}}{2\pi(1-\nu)k_BT}, \tag{5b}$$

$$h = \frac{c_{\mathrm{cl},1}}{\sqrt{\pi\rho}}. \tag{5c}$$

Here, h is the distance between dislocation dipoles. Using Eq. 5a in Eq. 3, v_cl is split into radiation-induced $v_{\mathrm{cl},r}$ and thermally-activated $v_{\mathrm{cl},t}$ components as

$$v_\mathrm{cl} = \left| v_\mathrm{cl,r} + v_\mathrm{cl,t}\left[\exp\left(\frac{Hb}{h}\right) - 1\right]\right|, \tag{6a}$$

$$v_\mathrm{cl,r} = \frac{1}{b}\left[(Z_I+\zeta_I)D_Ic_I - (Z_V+\zeta_V)D_V(c_V - c_V^e)\right], \tag{6b}$$

$$v_\mathrm{cl,t} = \frac{1}{b}\left[(Z_V+\zeta_V)D_Vc_V^e\right]. \tag{6c}$$

Note that in the absence of the deviation parameter ζ_ν, the irradiation climb velocity could vanish. This can be seen by considering the steady-state condition for point defects from Eqs. 1c,d. In the absence of point defect production bias or sinks other than dislocations, the steady-state is obtained as $Z_VD_V(c_V - c_V^e) = Z_ID_Ic_I$. Substituting this in Eq. 6b would result in $v_\mathrm{cl,r} = 0$. This situation has been discussed and addressed by Wolfer and Glasgow [3] by introducing the bias deviation $\alpha\zeta$ in Eq. 4.

The time for dislocation annihilation τ_cl was derived by Jourdan [4] by integrating the inverse of v_cl over the dipole distance as

$$\tau_\mathrm{cl} = \frac{h-b}{2v_\mathrm{cl,r}} - \frac{v_\mathrm{cl,t}Hb}{2v_\mathrm{cl,r}^2}\ln\left(\frac{\frac{v_\mathrm{cl,r}h}{v_\mathrm{cl,t}Hb}+1}{\frac{v_\mathrm{cl,r}b}{v_\mathrm{cl,t}Hb}+1}\right), \tag{7a}$$

$$\tau_\mathrm{cl} = \frac{h^2-b^2}{4v_\mathrm{cl,t}Hb} - \frac{v_\mathrm{cl,r}(h^3-b^3)}{6(v_\mathrm{cl,t}Hb)^2} \quad \text{for} \quad \frac{v_\mathrm{cl,r}h}{v_\mathrm{cl,t}Hb} \to 0, \tag{7b}$$

where the first expression applies to higher radiation damage levels and non-negligible radiation-induced

vacancy climb, while the second expression applies to lower radiation damage levels where radiation-induced vacancy climb is negligible. We refer to the above as Model 1.

Kohnert and Capolungo [2] recently derived improved expressions for the thermal recovery of dislocations by considering the collapse of an initial dislocation distribution. In evaluating the climb velocity, they accounted for the screening of stress fields by opposing forces from neighboring dislocations. Additionally, they considered the possibility that some dislocations (such as geometrically necessary dislocations) cannot recover by climb-mediated dipole annihilation, which we denote as ρ_{G}. The modified equations for annihilation rate and thermally-activated climb velocity in this model are given by

$$\left.\frac{d\rho}{dt}\right|_a = -\kappa_1(\rho-\rho_{\mathrm{G}})^{\frac{3}{2}}\sqrt{\frac{1-\frac{\rho}{\rho_\circ}}{1-\frac{\rho_{\mathrm{G}}}{\rho_\circ}}}v_{\mathrm{cl}}, \tag{8a}$$

$$v_{\mathrm{cl}} = v_{\mathrm{cl,t}}\exp\left[\frac{\kappa_2 G b^4(\rho-\rho_{\mathrm{G}})^{\frac{1}{2}}}{k_B T}\left(1-\frac{\rho}{\rho_\circ}\right)^{-\frac{1}{2}}-1\right], \tag{8b}$$

where κ_1 and κ_2 are constants. We refer to this as Model 2.

2.1.3. Dislocation Sink Strength

Faithful predictions of RIS and dislocation structure evolution requires an accurate description of the dislocation sink strength and its variation with dislocation density. Therefore, we tested the available analytical models and results derived from other modeling techniques. A solution to the non-dimensional sink strength or efficiency Z of edge dislocations is given by [4]

$$Z_\nu = 2\pi\sum_{n=0}^{\infty}(2-\delta_n)(-1)^n\frac{I_n\left(\frac{L_\nu}{2r_c}\right)I_n\left(\frac{L_\nu}{2R}\right)}{I_n\left(\frac{L_\nu}{2r_c}\right)K_n\left(\frac{L_\nu}{2R}\right)-I_n\left(\frac{L_\nu}{2R}\right)K_n\left(\frac{L_\nu}{2r_c}\right)}. \tag{9}$$

Here, $R=1/\sqrt{\pi\rho}$ relates to the dislocation spacing, making Z dependent on ρ. L_ν is the elastic interaction distance between the dislocation and a point defect, and is given in terms of the point defect relaxation volume

ΔV_ν as

$$L_\nu = \frac{1+\nu}{3\pi(1-\nu)} Gb \frac{|\Delta V_\nu|}{k_B T}. \tag{10}$$

Here, I_n and K_n are the modified Bessel functions of order n. Z_V and Z_I from Eq. 9 are plotted as a function of dislocation density in Fig. 2a. Parameters used to obtain the results of Fig. 2a are provided in Table 1. In the present work, Eq. 9 is used to perform zero-dimensional (0D) simulations of dislocation evolution in Sec. 2.3.1. Kohnert and Capolungo [2] carried out discrete dislocation dynamics simulations for body-centered cubic (BCC) Fe and compared the results of Z with a similar Bessel function-based analytical solution. They found the analytical solution to overpredict the sink strengths, especially at high dislocation densities. Therefore, there is uncertainty as to the accuracy of Z predicted by models such as Eq. 9. A common practice in rate-theory models for swelling and RIS has been to use constant values such as $Z_V = 1$ and $Z_I = 1.2$ (i.e. a bias of 20%) to simplify the description of the biased sinks. We use these simplified parameters to test the spatio-temporal model of RIS coupled with dislocation evolution in Sec. 2.3.2.

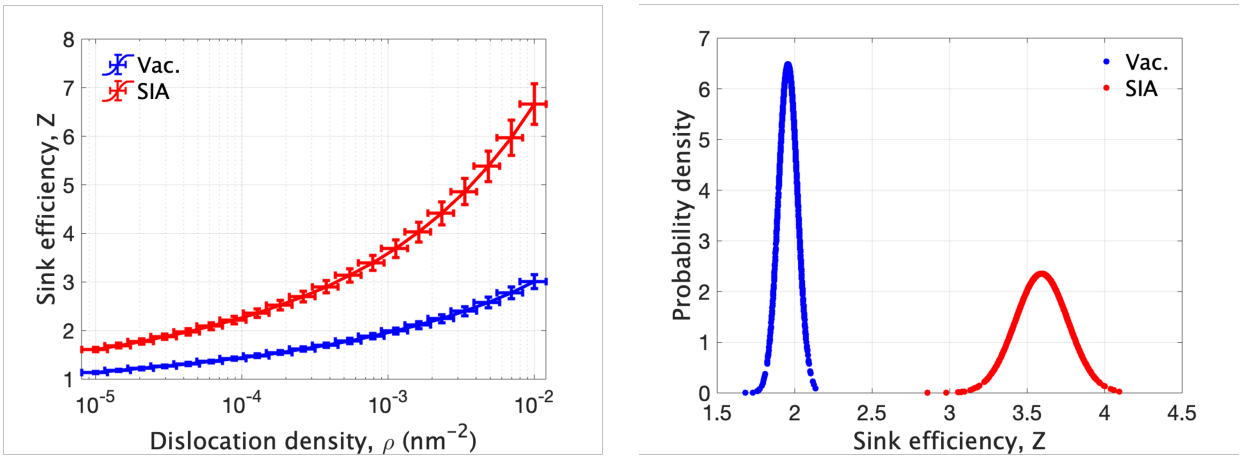

(a) (b)

Figure 2. (a) Analytical solution of dislocation sink efficiency Z as a function of dislocation density ρ for vacancy and SIA relaxation volumes of $\Delta V_V = -0.2V_a$ and $\Delta V_I = 1.8V_a$, respectively. (b) Probability density of Z for a normally distributed dislocation density of $\rho = 10^{-3}$ nm^{-2} and an assumed standard deviation of 0.2ρ.

Table 1. Parameters used in RIS and dislocation evolution models.

Symbol	Description	Value	Ref.
E_V^f	Vacancy formation energy	1.8 eV	[5]
S_V^f	Vacancy formation entropy	2 k_B	[6]
E_I^f	SIA formation energy	3.6 eV	[7]
E_I^m	SIA migration energy	0.6 eV	[5]
$E_{CrI}^b - E_{FeI}^b$	SIA binding energy for Cr	0.025 eV	[5]
$E_{NiI}^b - E_{FeI}^b$	SIA binding energy for Ni	-0.0075 eV	[5]
ω_{kI}°	SIA jump frequency prefactor	1.5×10^{12} s^{-1}	[7]
f_I	Atom-SIA correlation factor	0.44	[7]
$f_\circ$	FCC correlation factor	0.78	[8]
$a_\circ$	Lattice parameter	0.35 nm	[9]
b	Burgers vector	0.25 nm	[4]
λ_I	SIA jump distance	0.25 nm	[6]
V_a	Atomic volume	$a_\circ^3/4$	[6]
G	Shear modulus	77 GPa	[4]
ν	Poisson's ratio	0.29	[4]
r_c	Dislocation capture radius	$2b$	[4]
$r_\circ$	Recombination radius	$2a_\circ$	[6]
ΔV_V	Vacancy relaxation volume	-0.2V_a	[4]
ΔV_I	SIA relaxation volume	1.8V_a	[4]
$c_{\text{cl,1}}$	Constant in Model 1	$8\sqrt{3}$	[4]
$c_{\text{cl,2}}$	Free parameter in Model 1	0.6	[4]
l_{mesh}	Characteristic length	400 nm	[3]
κ_1	Parameter in Model 2	6.1	[2]
κ_2	Parameter in Model 2	0.58	[2]

2.2. Numerical Implementation

The model was implemented with the Multiphysics Object-Oriented Simulation Environment (MOOSE). For the spatially-resolved model, auxiliary phase-field order parameters η were employed to initialize a hexagonal sub-grain microstructure with approximately 100 nm sub-grain boundary width; this was realized using the Voronoi tessellation approach of Ref. [10]. Using thee order parameter fields, the as-solidified dislocation cell structure and composition distribution of the AM microstructure are generated as

$$\rho = \rho_{\text{bulk}} + (\rho_{\text{wall}} - \rho_{\text{bulk}}) \left[1 - \frac{1}{2}\left(1 + \tanh\left(\left(\chi - \chi_\circ\right)\beta_\circ\right)\right)\right], \tag{11}$$

$$c = c_{\text{bulk}} + (c_{\text{wall}} - c_{\text{bulk}}) \left[1 - \frac{1}{2}\left(1 + \tanh\left(\left(\chi - \chi_\circ\right)\beta_\circ\right)\right)\right]. \tag{12}$$

where $\chi = \sum_i \eta_i^2$, $\beta_\circ = 0.75$ and $\chi_\circ = \frac{2\tanh^{-1}(0.8)}{0.11}$ as defined in Ref. [11]. With this approach, dislocation cell walls with a uniform dislocation density of ρ_{wall} with a width of approximately 100 nm are realized. Computational complexity is minimized since the order parameters are only used to initialize the microstructure, as opposed to solving them as done in phase-field models. A finite element mesh employing quadrilaterals with 5 nm edge length was employed for the two-dimensional (2D) simulations. Weak forms of the partial differential equations were solved using implicit time and finite element spatial discretization. The non-linear equations were solved using Newton's method and a second order backward differencing scheme.

2.3. Results And Discussion

2.3.1. Mean-Field Dislocation Evolution

Parameters used in the model are provided in Table 1. Dislocation density-dependent sink efficiencies Z based on the analytical solution in Eq. 9 are employed. At both the cell wall and in the bulk, we assume a normal distribution of the dislocation density with a standard deviation of 0.2 times the mean. Using Eq. 9, the corresponding distributions and their standard deviations ζ are obtained as shown in Fig. 2. Note that similar to Z, ζ increases with ρ, with ζ_I increasing more strongly compared to ζ_V. Therefore, in addition

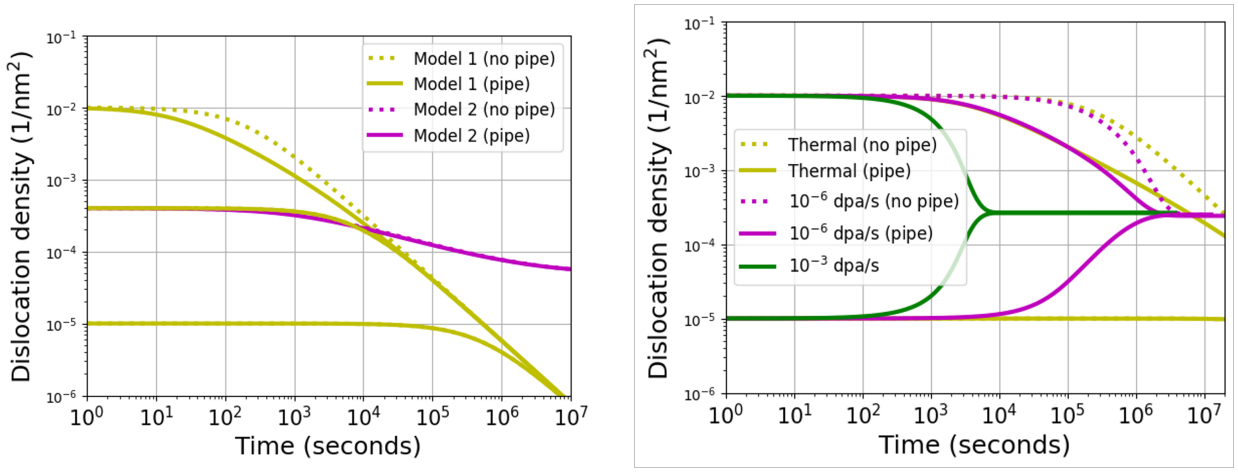

(a) (b)

Figure 3. Evolution of the dislocation density, ρ, under (a) thermal and (b) irradiation conditions from mean-field simulations with and without pipe diffusion. (a) Results for 1073 K for different starting ρ using Model 1 and 2. (b) Results for 873 K using Model 1.

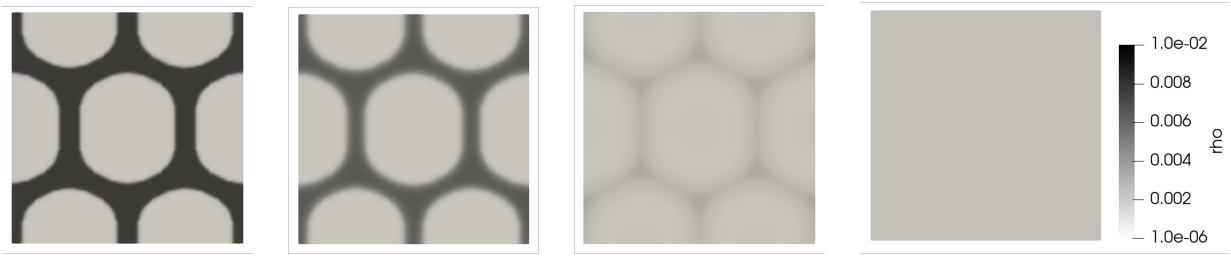

(a) (b) (c) (d)

Figure 4. Spatially-resolved 2D simulation of dislocation density, ρ, evolution under irradiation in a representative AM microstructure. Results correspond to irradiation at 773 K, 2×10^{-6} dpa/s and dose of (a) 0 dpa, (b) 0.02 dpa, or 2.8 hours, (c) 0.15 dpa, or 21 hours, and (d) 2 dpa, or 12 days.

to the increasing bias for SIA absorption, $(Z_I - Z_V)/Z_I$, the deviation in bias for SIA, $(\zeta_I - \zeta_V)/\zeta_I$, also increases.

In this section, we perform 0D simulations of the mean-field model for dislocation evolution. Fig. 3a shows dislocation recovery under thermal conditions at 1073 K from Model 1. While the recovery starts earlier for higher ρ, the recovery rates converge once steady state is achieved. At this high temperature, the pipe diffusion mechanism does not cause a significant difference to the recovery. For comparison, dislocation recovery under thermal conditions at a lower temperature of 873 K is shown in Fig. 3b. The recovery initiates later and the rate at steady state is slower. Additionally, pipe diffusion is seen to be significant. Fig. 3a also

shows the recovery from Model 2. Here, we assumed $\rho_G = 5 \times 10^{-5}$ nm^{-2} cannot recover. Results of this model shows slower recovery and a saturation dislocation density of ρ_G.

In addition to thermal recovery, Fig. 3b shows the effect of irradiation on enhancing dislocation recovery and generating new dislocation lines using Model 1. Saturation of dislocation density is observed under irradiation. The saturation value is observed to be relatively independent of the dose rate and is controlled by the parameter l_{mesh} [3] in Eq. 2b. A higher dose rate of 10^{-3} dpa/s is seen to accelerate the time to reach saturation.

2.3.2. Dislocation Cell Structure and RIS Evolution

In this section, we present the results of 2D simulations pertaining to spatially-resolved dislocation cell structures. We employed simplified sink strengths of $Z_v = 1$ and $Z_i = 1.2$ to test the performance of the model. Dislocation density-dependent deviation in the bias for SIA was implemented using Eq. 4. Fig. 4a shows the starting distribution of high dislocation density at cell walls and low dislocation density within the cells, representative of as-solidified AM microstructure. We first explore the evolution in the absence of GBs; this is the case where the dislocation sub-grain structure is within a large grain and far from the influence of GBs (e.g., solution-annealed material). Upon irradiation, the dislocations within cell walls recover while new dislocations are generated within the cell interior. As seen from Figs. 4b and c, the dislocation cells become less distinguishable with irradiation damage. At 2 dpa in Fig. 4d, the dislocation cell structure completely disappears as a homogeneous saturation density is reached.

The evolution of point defect concentrations and dislocation density at cell wall and cell interior (center) are plotted as a function of dose in Fig. 5a. The point defects are seen to rapidly reach a quasi-steady-state with distinct concentrations at cell walls and cell interiors. At this stage, a dynamic balance is achieved between point defect production and annihilation (due to recombination and dislocation absorption). The point defect concentrations are higher within the cells compared to the cell walls. At higher dpa, the dislocation densities evolve and reach a saturation value. Correspondingly, due to the changes in sink absorption rates, the point defect concentrations evolve to a new steady state. Here, c_V and c_I at cell wall increase due to a decrease in

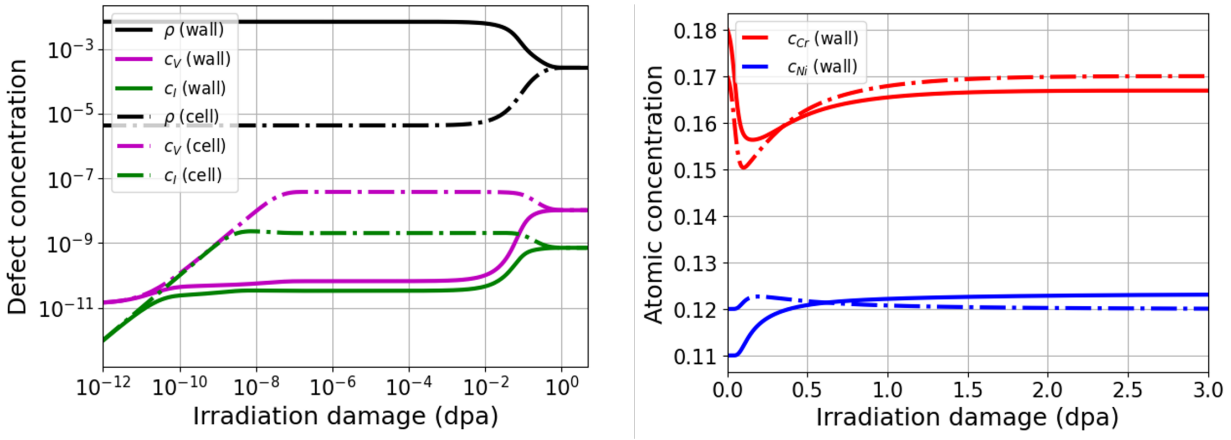

(a) (b)

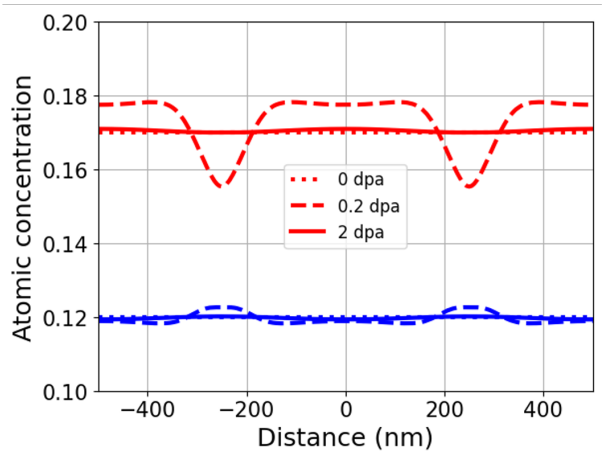

(c)

Figure 5. Plots of dislocation density (a), point defect (a) and atomic concentration (a,b) evolution with irradiation, within cell interior (cell) and at cell wall (wall). Results are obtained from the spatially-resolved 2D simulation shown in Fig. 4. (b) Cr (red) and Ni (blue) evolution starting from non-equilibrium pre-irradiation segregation. (c) Line profiles taken horizontally from the center of domain in Fig. 4.

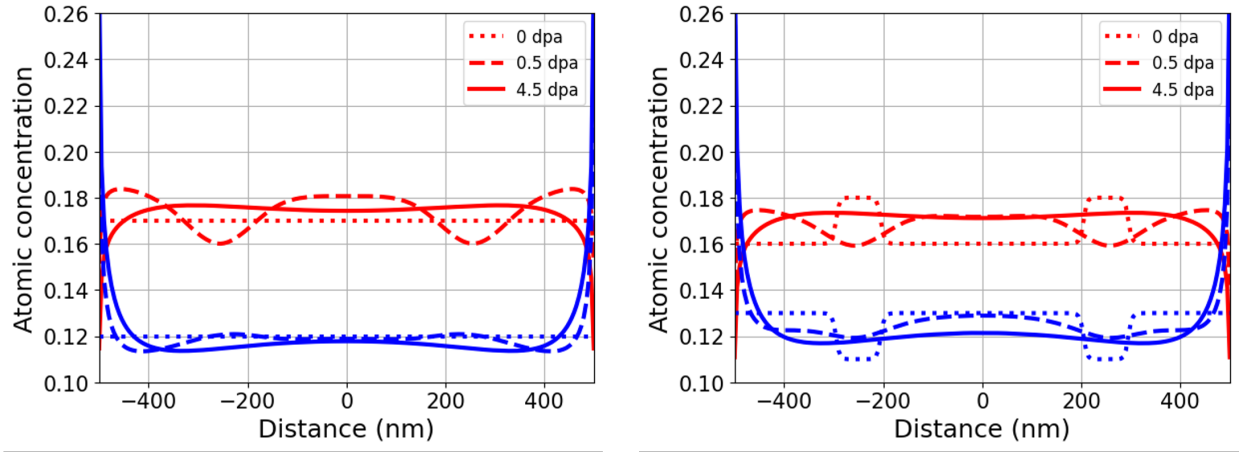

(a) (b)

Figure 6. Line profiles of Cr (red) and Ni (blue) concentrations taken horizontally from the center of a square grain similar to Fig. 4. An ideal GB is located at the edges of the domain. (a) Starting condition is of uniform composition. (b) Starting condition is an assumed non-equilibrium segregation.

ρ while the concentrations in the cell interior decrease due to the increase in ρ.

The evolution of Cr and Ni concentrations are plotted as a function of dose in Fig. 5b. Line profiles of the spatial variation taken horizontally from the center of the domain are shown in Fig. 5c for different doses. RIS is observed at the cell wall with Cr depleting significantly, Ni enriching slightly and the point defect concentrations being lower. However, with the recovery of dislocations at the cell wall, RIS also reduces as the sink strength decreases. Once the dislocation cell structure disappears, there is no spatial sink for point defects on an average at the length scale of the simulation. Thus, RIS vanishes, resulting in a homogeneous composition at 2 dpa.

Fig. 6a and b show the evolution of RIS in the presence of GBs at the edges of the square domain. RIS at the high angle GB is seen to be significantly greater than the RIS observed at the dislocation cell wall. This can be attributed to the higher sink strength of the GB compared to the dislocation cell wall. The absolute magnitude of Ni enrichment is observed to be greater than that of Cr depletion at the GB. This is in contrast to the slightly greater Cr depletion observed at the cell wall. The difference in magnitudes of Cr and Ni RIS at the cell wall results from the bias for SIA absorption. Starting from non-equilibrium pre-irradiation segregation consisting of Cr enrichment and Ni depletion at cell walls, Fig. 6b captures the transition to

Cr depletion and Ni enrichment under irradiation. While the biased dislocation sink is found to affect RIS directly, the variation in bias is observed to impact RIS via dislocation evolution.

2.4. Conclusions: Spatially-Resolved Microstructure Modeling

Mean-field models for line dislocation evolution were developed and coupled with spatially-dependent AM microstructures and rate-theory RIS using the MOOSE framework. The effect of pipe diffusion was found to be important to dislocation evolution and RIS at low temperatures. Compared to the classical model (Model 1) for the thermal recovery of dislocations, Model 2 predicts slower kinetics and appears more suited to the AM microstructure as it considers the collapse of a dislocation distribution and the possibility of dislocations that cannot recover. In fiscal year 2025, we plan to compare the model predictions with experimental data.

As Model 2 needs to be developed further for irradiation conditions, we tested Model 1 in the present work. In describing the dislocation climb velocity, the variation in sink strengths (or bias variance) arising due to the variation in dislocation density was found to be important. The results of this model captured the generation and enhanced recovery of dislocations under irradiation. Simulations of the spatially-resolved model demonstrated the decrease in cell wall dislocation density, the generation of new bulk dislocations, and the overall disappearance of the cell structure. RIS with Cr depletion and Ni enrichment was observed at the cell walls and grain boundaries, with the magnitudes being lower at the cell walls. Moreover, the relative extents of Cr and Ni RIS were found to be different at the cell walls due to their biased sink behavior.

The predictions of the models developed here are in good qualitative agreement with experimental observations. However, several uncertainties in the model lie in the parameterization of the pipe diffusion coefficient, dislocation generation, dislocation density distribution, point defect relaxation volumes and the deviation in sink strength as a function of dislocation density. With inputs on these parameters from atomistic and cluster dynamics models, a quantitative simulation capability for radiation- and thermally-induced AM microstructure evolution that can be validated with experimental characterization will be developed.

3. MEAN-FIELD MICROSTRUCTURE MODELING

3.1. Motivation

AM 316 stainless steels are of interest for use as structural materials in next-generation nuclear reactors. They exhibit microstructural features such as cellular dislocation structures, compositional segregation due to solidification, and precipitates, that influence their irradiation behaviour significantly [12–16]. The complex network of different microstructure sinks determine the population of predominant irradiation defects at different irradiation conditions. The population of such defects and their spatial distribution determine the micro- and macro-mechanical properties of such steels under reactor operation conditions. Reaction rate theory-based mean-field cluster dynamics (CD) models have been widely used to predict the population of irradiation-induced defects in materials [17–20]. We have implemented a similar mean-field CD framework for 316 steels, implementing the model and the parameters presented by Pokor et al. [20]. A successful implementation of this mean-field CD framework lays the foundation for an improved CD model with reaction species and spatially inhomogenous microstructural sinks, specific to AM 316 steels.

3.2. The Mean-Field Cluster Dynamics Framework

3.2.1. Background of the Mean-Field Cluster Dynamics Model

The mean-field CD model assumes a homogenous density of irradiation defects, i.e., Frenkel pairs, voids, dislocation loops and small self-interstitial atom and vacancy clusters in the matrix, without any spatial fluctuation. This is a reasonable approximation to examine aggregated bulk-like behaviors, as the spatial fluctuations in defect densities are negligible in the matrix except near microstructural sinks, i.e., line dislocations and dislocation cell walls, grain and subgrain boundaries, cavities, precipitates and free surfaces. Such fluctuations are a consequence of the varying free energies of defect formation and migration in the vicinity of sinks, due to elastic distortion in the matrix. The effect of such spatially discrete microstructure sinks on the homogenous density of irradiation defects is incorporated in the mean-field CD framework using

an 'effective medium' assumption. Under this assumption, the spatially discrete sinks are homogenously smeared out in the entire matrix. The flux of irradiation defects at the interface between matrix and the discrete sink surface is replaced with an equivalent reaction rate term, given as a product of the rate coefficient and the homogenous concentration of the sinks and interacting defect. Details about the mean-field CD framework and the treatment of discrete sinks have been discussed in the works by Brailsford et al. [21]. Under the 'effective medium' approximation, discrete displacement cascade events are also smeared out across the entire matrix, resulting in a spatially homogenous term for the generation of point defects and small clusters.

3.2.2. The Cluster Dynamics Model

To adopt the mean-field CD approach to predict the evolution of irradiation-induced defects in AM 316 steels, the spatially inhomogenous AM microstructure must be defined in a way that can be provided as input to the CD model. Features of the AM microstructure, such as the dislocation cell walls, the network dislocation within the cells, and precipitates acts as strong sinks to defects. As a first iteration, we can spatially homogenize the dislocation density in the cell walls and the network dislocation density within the cells into an average value, $\langle\rho\rangle$, and use it as an effective dislocation sink density in the CD model. Similarly, an average density of precipitates can be introduced as sinks. However, a more rigorous approach would be to define the average density of dislocation cell walls as $\langle\rho_{cw}\rangle$ and the average density of network dislocations within the cells $\langle\rho_n\rangle$. Phenomenological equations defining the sink strengths of the cell walls towards point defects must be defined. In addition, the interaction of cell walls with point defects resulting in a climb-glide mechanism of the dislocations at the cells walls and their eventual transformation into network dislocations must be accounted for in the CD model using separate rate equations for $\langle\rho_{cw}\rangle$ and $\langle\rho_n\rangle$.

The CD model is based on reaction-rate theory where the density of each defect species, i.e., SIAs, vacancies, and loops of each size, is evolved using rate equations. The rate equations are defined as a sum of the rates of generation and annihilation of such defects due to possible interaction with other defects and microstructural sinks. A source term is also added to the rate equations, for the point defects and small defect clusters generated in the displacement cascade. Thus, the governing equations of the model are [20]:

$$\frac{dC_i(n)}{dt} = G_i(n) + a_{i,n+1}C_i(n+1) - b_{i,n}C_i(n) + c_{i,n-1}C_i(n-1), \tag{13a}$$

$$a_{i,n+1} = \beta_{i,v}(n+1)C_v(1) + \alpha_{i,i}(n+1), \tag{13b}$$

$$b_{i,n} = \beta_{i,v}(n)C_v(1) + \beta_{i,i}(n)C_i(1) + \alpha_{i,i}(n), \tag{13c}$$

$$c_{i,n-1} = \beta_{i,i}(n-1)C_i(1). \tag{13d}$$

$$\frac{dC_i(1)}{dt} = G_i(1) - R_{iv}C_i(1)C_v(1) - \frac{C_i(1)}{\tau^a_{d,i}} - \frac{C_i(1)}{\tau^a_{gb,i}} - \frac{C_i(1)}{\tau^a_i(n)} + \frac{1}{\tau^e_i(n)}, \tag{14a}$$

$$\frac{1}{\tau^e_i(n)} = \sum_{n>2} \alpha_{i,i}(n)C_i(n) + 4\alpha_{i,i}(2)C_i(2) + \beta_{i,v}(2)C_vC_i(2), \tag{14b}$$

$$\frac{1}{\tau^a_i(n)} = \sum_{n>0} \beta_{i,i}(n)C_i(n) + \sum_{n>1} \beta_{v,i}(n)C_v(n). \tag{14c}$$

$$\frac{d\rho}{dt} = -Kb^2\rho^{3/2}. \tag{15}$$

In Equation 13a, $C_i(n)$ is the density of SIA loops of size n. The equation is a sum of the source term for such defects, i.e., $G_i(n)$, the rate of absorption of SIAs by small SIA loops creating an n-sized loop, and the rate of depletion in the density of n-sized loops, due to emission of SIAs from loops and the rate of absorption of vacancies by SIA loops. The rate coefficient for absorption of SIA and vacancies by SIA loops are given as $\beta_{i,i}(n)$ and $\beta_{i,v}(n)$, respectively. The rate coefficient for emission of SIAs from SIA loops is given as $\alpha_{i,i}(n)$. Equation 14a defines the evolution of SIA density, $C_i(1)$, as a sum of the rate of generation in the cascade, depletion due to recombination with vacancies, and absorption by dislocations, grain boundaries and SIA loops, and rate of creation due to thermal emission from SIA loops. R_{iv} is the coefficient of mutual recombination between SIA and vacancies. Similar equations are defined for vacancies

and vacancy loops. Equation 15 defines the evolution of dislocation sinks, due to climb-glide mechanism facilitated by the absorption of point defects in the displacement cascade. For further details on the model, the readers are directed to the work by Pokor et al. [20].

3.2.3. The Rate Coefficients of the CD Model

The interaction between defects in the irradiated matrix is diffusion-controlled and the kinetics is governed by the diffusivity of the diffusing species. An important assumption of this CD model is that the point defects, i.e., the SIAs and the vacancies, are the only mobile diffusing species in the irradiated matrix. Thus, in Equations 16a and 17a, the rate coefficient for mutual recombination, the absorption of point defects by dislocation and grain boundary sinks, and the absorption and emission coefficients are all governed by the diffusivity of SIAs and vacancies, i.e., D_i and D_v, respectively. The coefficient of thermal emission of point defects from the loop is also governed by the binding energy associated with the absorption of point defects to respective loops, i.e., $E_{bi}(n)$ and $E_{bv}(n)$. Finally, the coefficient of absorption of point defects to loops, i.e., $\beta_{i,i}(n)$, $\beta_{i,v}(n)$, $\beta_{v,v}(n)$, $\beta_{v,i}(n)$, also depends on the capture efficiency of the loops for the point defects, i.e., Z_{iC} and Z_{vC}.

$$R_{iv} = 4\pi(D_i + D_v)r_{i,v}, \tag{16a}$$

$$\frac{1}{\tau^a_{d,i}} = \rho D_i Z_i, \tag{16b}$$

$$\frac{1}{\tau^a_{gb,i}} = 6D_i \frac{\sqrt{\rho_D Z_i + \sum_n \beta_{i,i}(n)C_i(n) + \sum_n \beta_{v,i}(n)C_v(n)}}{d}. \tag{16c}$$

$$\alpha_{i,i}(n) = 2\pi r_i(n) Z_{ic} \frac{D_i}{V_{at}} \exp\left(-\frac{E_{bi}(n)}{kT}\right), \tag{17a}$$

$$\beta_{i,i}(n) = 2\pi r_i(n) Z_{ic} D_i, \tag{17b}$$

$$\beta_{i,v}(n) = 2\pi r_i(n) Z_{ic} D_v, \tag{17c}$$

$$\alpha_{v,v}(n) = 2\pi r_v(n) Z_{vc} D_v \exp\left(-\frac{E_{bv}(n)}{kT}\right), \tag{17d}$$

$$\beta_{v,v}(n) = 2\pi r_v(n) Z_{vc} D_v, \tag{17e}$$

$$\beta_{v,i}(n) = 2\pi r_v(n) Z_{ic} D_i. \tag{17f}$$

3.2.4. Parameters of the Model

As mentioned above, the diffusivities of SIAs and vacancies govern the kinetics of loop evolution. The diffusivities can be further parameterized with the pre-exponential diffusivity factor, D_i° and D_v°, and the migration energy of point defects, E_i^m and E_v^m. Similarly, the capture efficiency can be parameterized using Equation 19 where Z_i, b, a and n are the capture efficiency of line dislocations towards point defects, Burgers vector of loops, lattice parameter and loop size, respectively. Z_{1i} and a_{1i} are fitted coefficients in Equation 19. Finally, using a capillarity law, the binding energy of point defects to loops can be parameterized using Equation 20, where E_{fi} and E_{b2i} are the formation energy of point defects and dimers, respectively. For further details about the parameters, the readers are directed to the prior CD works [18–20]. A list of the the parameters used for the CD simulations can be obtained in the work by Pokor et al. [20].

$$D_i = D_i^\circ \exp\left(-\frac{E_i^m}{kT}\right), \tag{18a}$$

$$D_v = D_v^\circ \exp\left(-\frac{E_v^m}{kT}\right). \tag{18b}$$

$$Z_{ic} = Z_i + \left(\sqrt{\frac{b}{8\pi a}} Z_{1i} - Z_i\right)\left(\frac{1}{n^{a_{1i}}}\right). \tag{19}$$

$$E_{bi}(n) = E_{fi} + \frac{E_{b2i} - E_{fi}}{2^{0.8} - 1}(n^{0.8} - (n-1)^{0.8}) \tag{20}$$

3.3. Results And Discussions

3.3.1. Simulation Conditions

Using the CD model provided above, the evolution of SIA and vacancy loops were studied in cold-worked 316 (no distinction made for L or H sub-designations) stainless steels [20] subject to the different irradiation temperatures and dose rates. In addition, the dislocation sink density was varied to study its effect on the loop population evolution. Table 2 lists the CD simulation conditions.

T (°C)	dose rate (dpa/s)	ρ (m^{-2})
$350, 450, 550$	$10^{-2}, 10^{-4}, 10^{-6}$	$10^{12}, 10^{16}$

Table 2. CD simulation conditions.

The choice of CD simulation conditions corresponds to the actual conditions during irradiation experiments. The chosen irradiation temperatures fall within the operational temperature window of advanced nuclear reactors. The choice of dose rates emulates different irradiation conditions, i.e., ion-irradiation with high dose rates and neutron irradiation with a dose rate of $10^{-6} - 10^{-7}$ dpa/s. The choice of dislocation sink densities correspond to an annealed 316L steel sample with low dislocation density of 10^{12} m^{-2} and a cold-worked 316L sample with a high density of 10^{16} m^{-2}. A high density of dislocation sinks of a similar magnitude is also observed in AM 316L [14, 16]. Thus, the CD model can be used to predict the evolution of irradiation defect populations for different experimental conditions and material parameters. The current version of the CD model considers a constant density of dislocation sinks which does not evolve as the irradiation progresses. In other words, Equation 15 has not been included in the current model. Future versions of the model would also include the proper physics for dislocation sink evolution with irradiation. Also, the interaction of point

defects with grain boundaries have been neglected in the model.

3.3.2. Evolution of Dislocation Loops

The predicted populations of SIA and vacancy loops have been presented in Figures 7 and 8. The population of SIA and vacancy loops have been characterized by the total density of loops, their average diameter and size distribution plots (SDPs). The predicted evolution of the total loop density in annealed 316L, with irradiation dose, at $350°$C and 10^{-2} dpa/s has been presented in Figure 7a. The solid lines represent the total density of SIA and vacancy loops, indicated by ni and nv respectively, while the dotted and dashed lines represent the density of small loops with diameter ≤ 1 nm, and large loops with diameter > 1 nm, respectively. Evolution of the average diameter of loops is presented in Figure 7b. Similarly, the dotted, dashed and solid lines represent the average diameter of small, large and all loops, respectively. The important observations are:

- During the initial stages of irradiation, at very low doses, there is an accumulation of very small SIA and vacancy loops. This is observed from the constant increase in small loop densities up to a dose of 10^{-8} dpa.
- The SIAs being more mobile than the vacancies, start diffusing at around 10^{-8} dpa, initiating SIA loop growth. The change in slope of the SIA loop density plot, at the same dpa, indicates an onset of SIA loop growth. Small vacancy loops still keep accumulating in the irradiated matrix.
- The growth of SIA loops continue with irradiation reaching large sizes, i.e., > 1 nm, which can be observed from the dashed line in Figure 7a.
- The density of large SIA loops eventually overtakes the density of small SIA loops at around 10^{-3} dpa, in Figure 7a. As a result, we observe a significant coarsening of SIA loops from the plot of average loop diameter, i.e., Figure 7b.
- The sluggish mobility of vacancies restricts the extensive growth of vacancy loops. As a result, we see the constant accumulation of small vacancy loops as compared to the small density of large vacancy loops, in Figure 7a.
- The corresponding SDPs for SIA and vacancy loops are shown in Figure 8a and b, respectively. The growth

and coarsening of SIA loops is characterized by the shifting of the peak of SDP plots to larger loop sizes. Conversely, the accumulation of small vacancy loops results in a SDP having a peak at small loop sizes. The vacancy loop SDP does not show any significant shift to higher loop sizes upon irradiation.

3.3.3. Effect of Temperature on Loop Evolution

Temperature has significant effect on the evolution of irradiation-induced SIA and vacancy loops with dose. The diffusivity of mobile SIAs and vacancies increases with temperature, which can accelerate the growth and coarsening of loops due to absorption of mobile point defects. However, an enhanced diffusivity of point defects also accelerates the rate of mutual recombination between SIAs and vacancies and the rate of absorption of unlike point defect by loops, leading to their annihilation. Thus, loop growth and point defect annihilation are competitive mechanisms which determine part of the overall behavior of the material under irradiation at this temperature.

At a dose rate of 10^{-4} dpa/s (Figure 9b), the competition between point defect annihilation and loop growth is observed clearly. At low temperature, i.e., $350°C$, the onset of the regime where SIA loop growth competes with point defect annihilation is seen from the plateau in the total density of SIA loops, indicated using the solid black line. As irradiation progresses, more point defects become available in the matrix, allowing the rate of SIA loop growth to overtake the rate of point defect annihilation, resulting in extensive loop growth at around 10^{-4} dpa. The onset of extensive loop growth can also be observed from the plot of average SIA loop density with dose in Figure 10b. At around 10^{-4} dpa, the average SIA loop diameter begins to steadily increase.

An increase in the irradiation temperature results in an early onset of the competition between SIA loop growth and point defect annihilation. This can be seen from the onset of the plateau regime for SIA loop densities at different temperatures (Figure 9b). In addition, an increase in temperature extends the plateau regime to higher doses, restricting the extensive coarsening of loops due to accelerated point defect annihilation. This is a consequence of the enhanced diffusivity of SIAs and vacancies at high temperatures. The plateau regime is also observed in the plots for the total density of vacancy loops with dose. However,

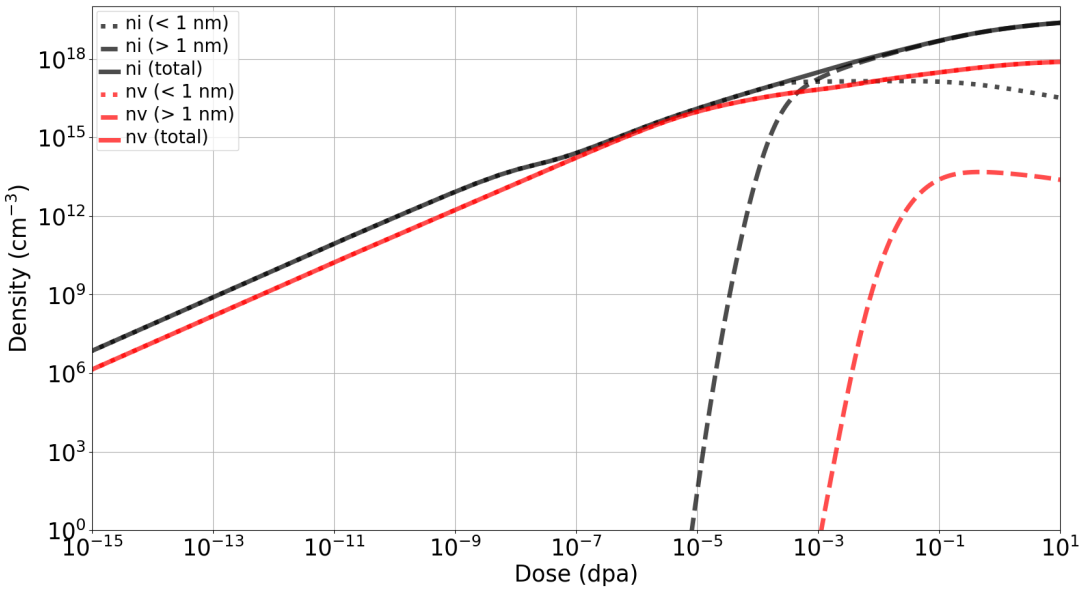

(a)

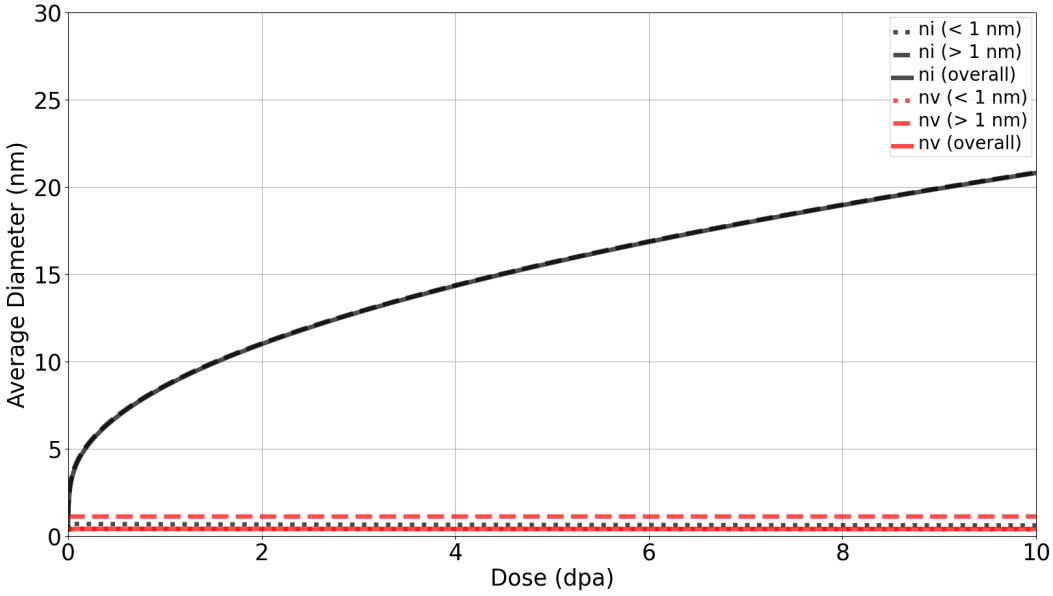

(b)

Figure 7. Evolution of the (a) total density and (b) average diameter of SIA and vacancy loops with dose, using a dose rate of 10^{-2} dpa/s at 350°C. In addition, the total density and average diameter of the small loops ($<$ 1 nm) have been computed separately from those of the large loops ($>$ 1 nm).

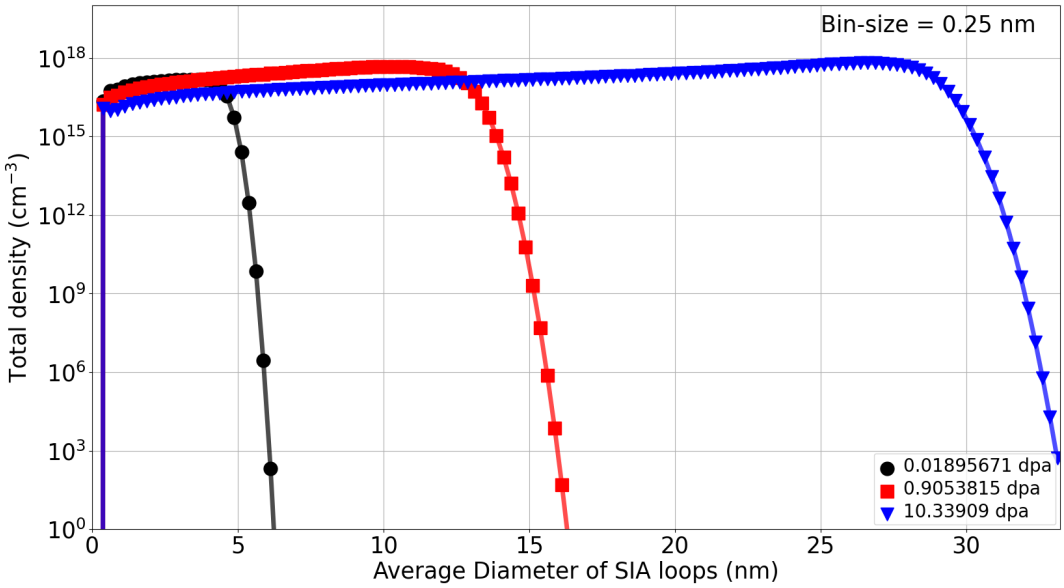

(a)

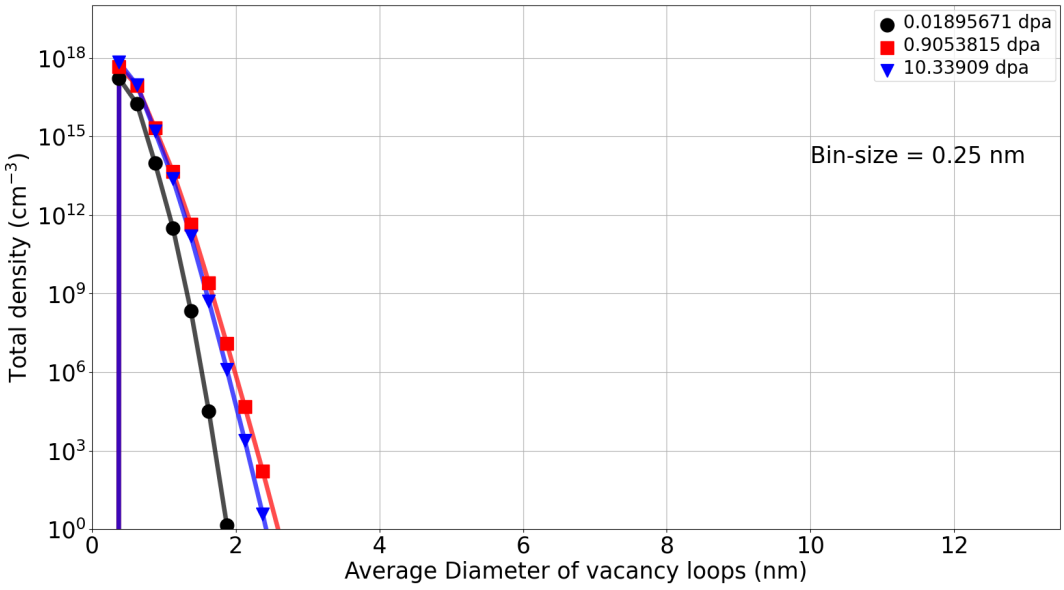

(b)

Figure 8. Evolution of the size distribution plots of (a) SIA and (b) vacancy loops at different doses, using a dose rate of 10^{-2} dpa/s at 350°C. These are histogram plots with size bins = 0.25 nm.

the vacancy loops do not undergo extensive growth beyond this regime of competition. A similar trend in the evolution of the void population with temperature and irradiation dose is also observed at a dose rate of 10^{-6} dpa/s, as shown in Figures 9c and 10c.

3.3.4. Effect of Irradiation Dose Rate on Loop Evolution

The irradiation dose rate affects the vacancy loop population evolution. A high irradiation dose rate results in a larger density of available point defects in the irradiated matrix. As a result, the point defects do not have time to diffuse and interact with each other and with loops. Thus, the accumulation of small SIA and vacancy loops continue until high dose values. Figure 9a shows the evolution of the total SIA and vacancy loop density at 10^{-2} dpa/s. At all temperatures, there is a significant accumulation of small loops until the onset of the plateau regime at higher dose values. This can be inferred from a comparison of Figure 9b with Figure 9a for SIA loop density evolution at all temperatures.

An increase in the available point defects due to a high dose rate also helps to overcome the regime of competition between SIA loop growth and point defect annihilation. An increased density of available and mobile point defects increases their rate of absorption by loops as compared to the rate of mutual annihilation. This promotes an early onset of the loop coarsening after overcoming the plateau regime. Comparing the extent of the plateau regime in the SIA loop density plots of Figure 9b and a for all temperatures clearly indicates the discussed mechanism. The early onset of loop coarsening is also evident from the plot of average loop diameter at 10^{-2} dpa/s, in Figure 10a.

At high dose rate and temperature, the density of available point defects as well as their diffusivities are enhanced. This results in both the above mentioned effects, i.e.,

- accumulation of small loops and a delayed onset of the plateau regime where loop growth competes with point defect annihilation,
- early onset of loop coarsening by easily overcoming the plateau regime. SIA loop evolution at 10^{-2} dpa/s and $550°C$, in Figures 9a and 10a, shows both the characteristics features.

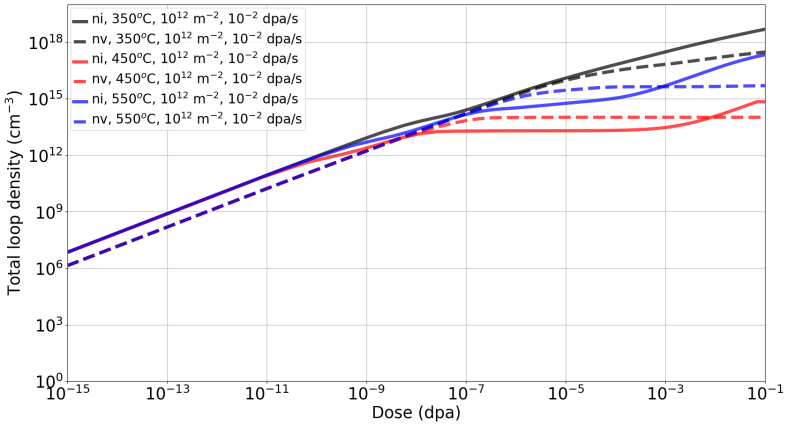

(a)

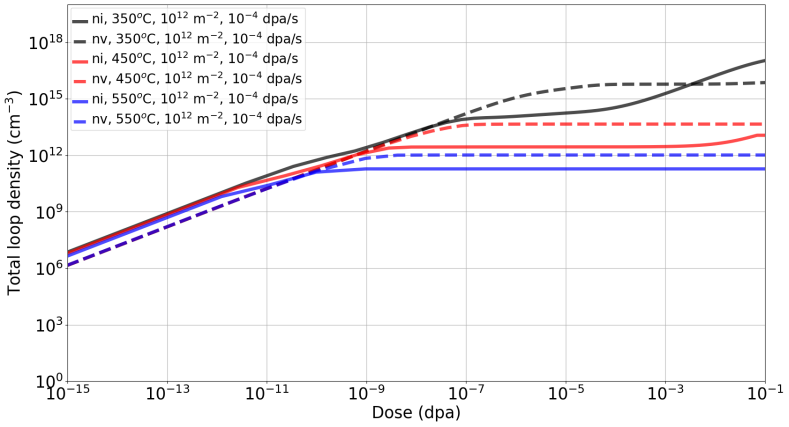

(b)

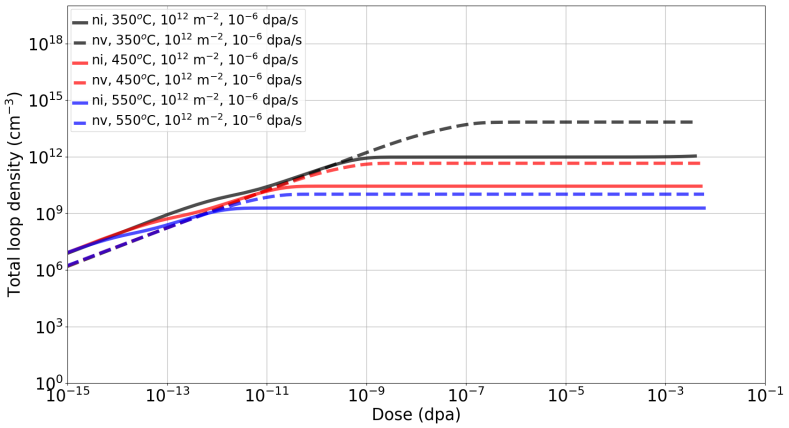

(c)

Figure 9. Evolution of the total density of SIA and vacancy loops, with dose, at $350, 450, 550$°C for an irradiation dose rate of (a) 10^{-2}, (b) 10^{-4} and (c) 10^{-6} dpa/s.

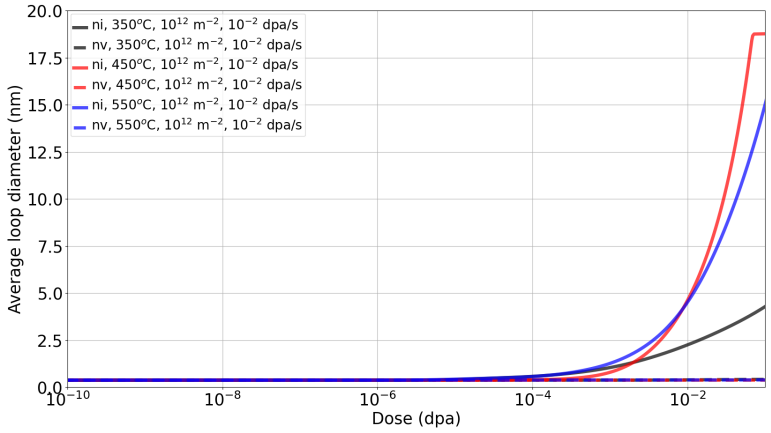

(a)

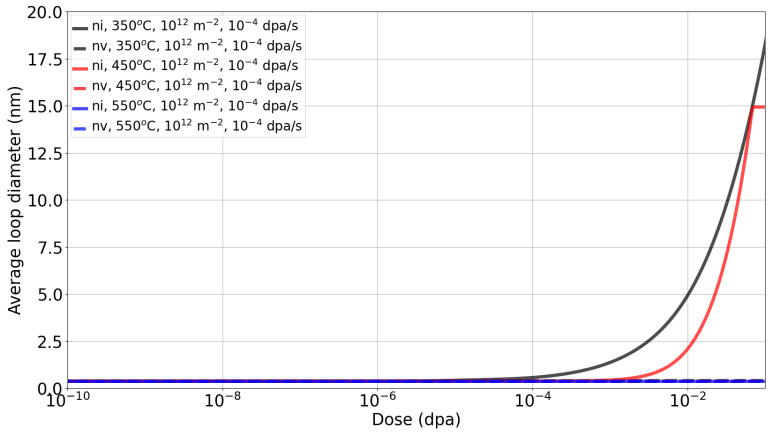

(b)

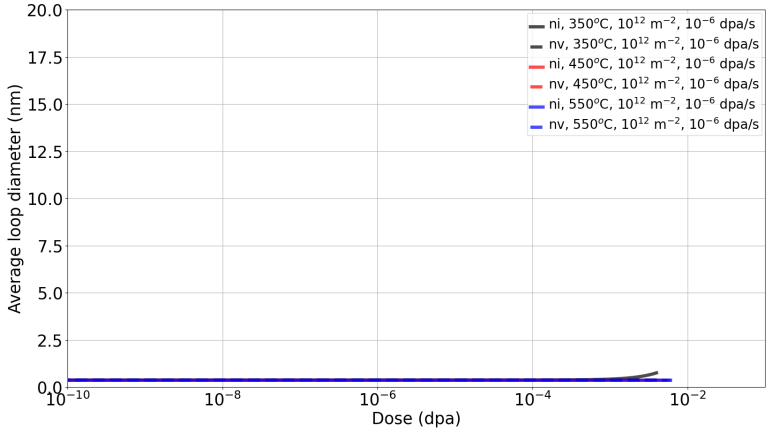

(c)

Figure 10. Evolution of the average diameter of SIA and vacancy loops, with dose, at $350, 450, 550$°C for an irradiation dose rate of (a) 10^{-2}, (b) 10^{-4} and (c) 10^{-6} dpa/s.

3.3.5. Effect of Network Dislocation Sink Density on Loop Evolution

The presence of network dislocations that act as sinks significantly depletes the density of mobile point defects. In this model, network dislocations are sinks that are non-saturable and have a constant sink strength. As a result, the coarsening of SIA loops is restricted, further extending the plateau regime. This is evident from Figures 11a and b. At a sink density of $10^{12}\mathrm{m}^{-2}$, the coarsening of SIA loops continue after the plateau regime in the plot of SIA loop density with dose. Increasing the sink density to 10^{16} m^{-2} accelerates the annihilation of mobile SIAs at the sink. This restricts the SIA loop coarsening significantly, as evident from Figure 11b. Consequently, this promotes the accumulation of small vacancy loops in the matrix. The density of vacancy loops is about two orders of magnitude higher than the density of SIA loops at a high sink density of 10^{16} m^{-2} in Figure 11a.

3.4. Conclusion: Mean-Field Microstructure Modeling

We have presented a mean-field cluster dynamics model that can be effectively used to predict the evolution of irradiation defects in additively manufactured 316 stainless steel, which is a crucial capability in being able to combine ion and neutron irradiation testing for accelerated material qualification. In the current model, the irradiation defects considered are the SIA and vacancy dislocation loops, based on the work by Pokor et al. [20]. The predicted evolution of the loop population shows growth and coarsening of large SIA loops and an accumulation of small vacancy loops without any significant growth due to the sluggish kinetics of vacancies, which restricts their diffusion and migration to loops and sinks, even at high temperature and irradiation dose rates. The crucial effect of temperature, irradiation dose rate and density of dislocation sinks, on the evolution of loop population, were discussed in detail. Significantly, the CD model predictions of loop growth versus temperature at a given damage rate have good qualitative agreement with ion irradiation results from within the AMMT program (i.e., rapid onset of loop formation at $350°\mathrm{C}$, while loop formation is suppressed until higher damage levels at $650°\mathrm{C}$). In addition, the CD model sheds light on the effect of dislocation sinks on the evolution of loops. SIA loop growth is suppressed at a high dislocation sink density,

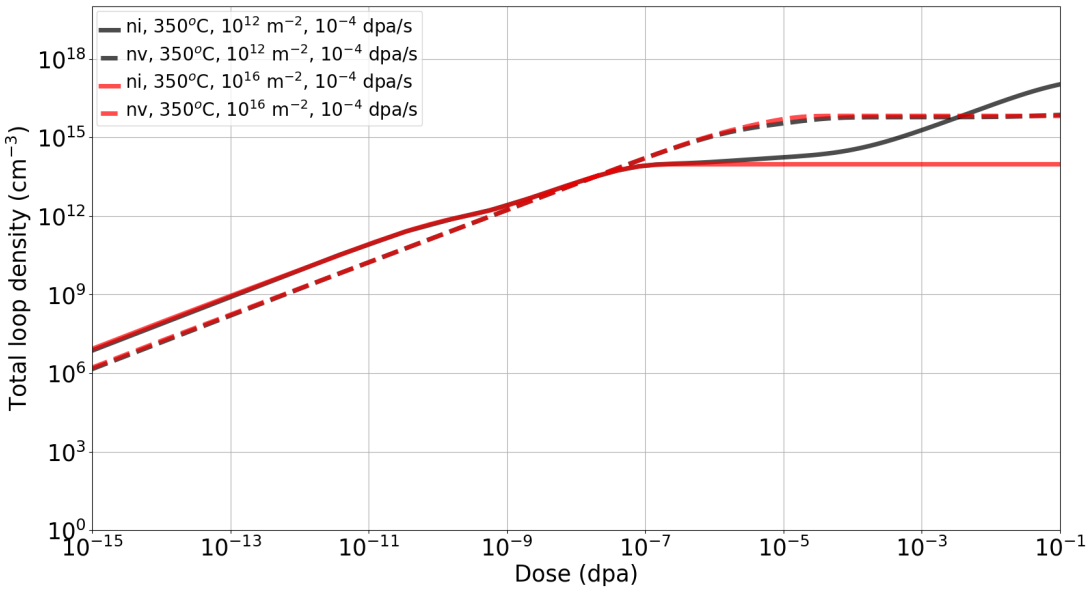

(a)

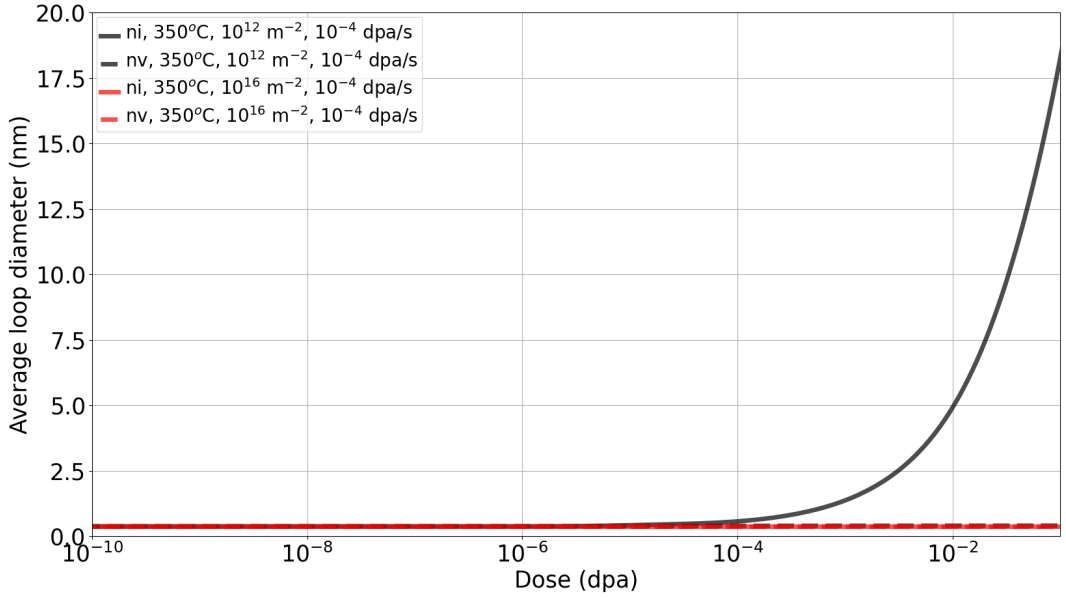

(b)

Figure 11. Evolution of (a) the total density and (b) average diameter of SIA and vacancy loops, with dose, at different dislocation sink densities, i.e., 10^{12} and 10^{16} m^{-2}. The temperature and irradiation dose rates are 350°C and 10^{-4} dpa/s, respectively.

promoting an almost two order of magnitude increase in the number of small vacancy loops in the matrix. A similar observation is also expected for the presence of voids in AM 316. Concurrent evolution of network dislocation sinks, with SIA and vacancy loops, can also be included in the CD model, which will allow us to study the evolution of dislocation sink density with a climb-glide mechanism due to the migration of SIA and vacancies generated in the displacement cascade.

However, the current version of the model has certain limitations, making validation with experimental results somewhat challenging. Currently, it is difficult to predict the evolution of large SIA loops, > 30 nm, at high irradiation doses of $\sim 10 - 100$ dpa, for neutron irradiation conditions, i.e., a low dose rate of $\sim 10^{-6} - 10^{-7}$ dpa/s. This challenge is results from the computationally expensive nature of the CD model. The equations of the model are discrete ordinary differential equations with each equation representing the evolution of each SIA or vacancy loop of a specific size. Thus, reaching the size ranges of defects observed in irradiation experiments requires around $\sim 10^5$ discrete non-linear equations being solved simultaneously. Efficient scaling can be achieved by utilizing grouping techniques as proposed by Kiritani [22] and later improved by Golubov et al. [23] and Kohnert et al. [24].

4. ATOMISTIC MODELING

4.1. Molecular Dynamics Introduction

Atomistic modeling is a set of techniques that allows us to build our understanding of the atomic scale phenomena associated with the generation and evolution of irradiation-induced defects in materials such as 316 stainless steel. These lower length scale techniques, such as molecular dynamics (MD), allow us to study both the energetics and kinetics of atomistic-scale phenomena such as primary radiation damage and the growth of irradiation-induced defects, in order to parameterize higher length scale cluster dynamics and phase field models. Additionally, it has been observed in previous experimental work that variation in the material composition strongly influences the evolution of irradiation induced defects over time, providing additional motivation to investigate the underlying mechanisms.

In this section, we use MD simulations to calculate the formation energy of various types of defect clusters and the rate at which these energies increase with the increasing size of the defect cluster. Atomistic simulations were also performed to calculate the interaction energy between voids and nearby vacancies to study the sink strength of voids. Additionally, both diffusional simulations and energetic studies investigating the interaction between groups of vacancies and carbon atoms were performed to learn more about how the carbon content slows the growth of voids in this material system.

4.2. Modeling 316 Stainless Steel Via Molecular Dynamics

MD is a technique for modeling the behavior of a system consisting of an ensemble of atomic particles using the classical Newtonian equations of motion. The motion of each atom in the simulation is tracked through time by determining the forces acting upon it, using an interatomic potential, and numerically integrating in time to obtain its position at the next time step of the simulation. In this work, MD simulations were performed using the Large scale Atomistic/Molecular Massively Parallel Simulator (LAMMPS) software, an open source package developed by Sandia National Laboratories [25] that is highly optimized for running MD simulations across many computing cores. Two different MD potentials were used to model the behavior of 316 SS, either a Tersoff [26, 27]-based interatomic potential used to create a model Fe-Cr-C systems or an embedded atom method (EAM) interatomic potential [28, 29] used to create a model Fe-Cr-Ni system. To represent 316 SS, a composition of 17 wt% Cr, 12 wt% Ni, and 0.04 wt% C were used when applicable, with the remaining balance made up of Fe. Model alloys were based on a FCC lattice, with the element of each atom randomly selected to recreate the target composition. Carbon atoms were randomly distributed into ternary sites in the FCC lattice.

4.3. Formation Energy Of Defect Clusters

An important component of understanding the evolution of irradiation-induced defects in a material is the formation energy of the commonly occurring defect clusters and how these formation energies scale with the number of point defects contained within the defect cluster. This information allows us to understand what

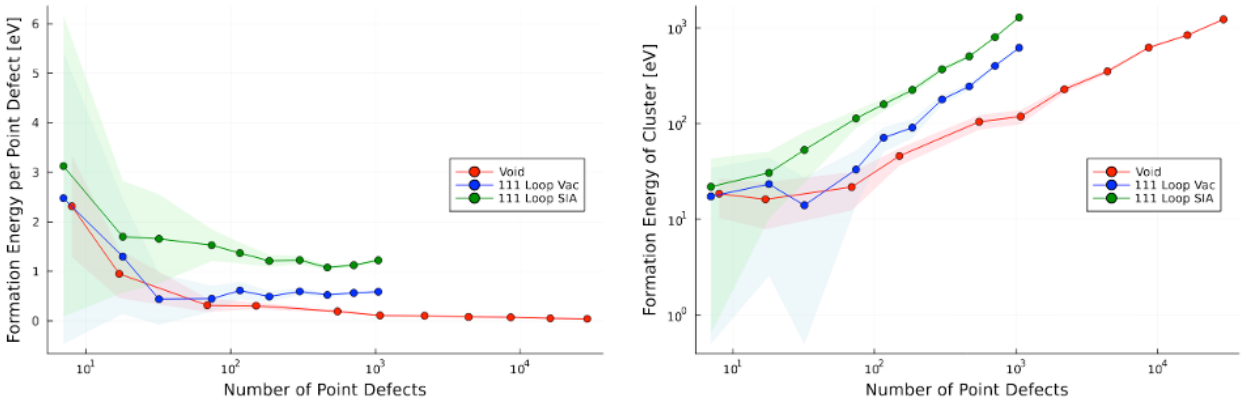

(a) (b)

Figure 12. Formation energy calculated for voids (red), <111> vacancy loops (blue), and <111> SIA loops (green). The shaded region corresponds to one standard deviation around the mean value. a) Plot of the average formation energy of the point defects making up the defect cluster. b) Plot of the total formation energy of each cluster type as a function of the number of point defects in the cluster.

defect structures have the highest stability and are the most likely to occur in the material, which provides greater insight into experimental results obtained from irradiation experiments of 316 stainless steel.

To evaluate the formation energy of defect structures, MD simulations were created to compare the potential energy of a perfect FCC lattice of the Fe-Cr-C model with a lattice containing either a SIA <111> loop, a vacancy <111> loop, or a spherical void. The initial atomic configurations of these defect structures were created using the AtomSK software package [30]. The resulting initial configurations were then run through a short energy minimizing routine prior to running an MD simulation for 5 ps. Simulations of spherical voids were performed at a temperature of 27°C, 300°C, and 600°C. Simulations of <111> loops were performed at a temperature of 100 K to improve the stability of the loops and minimize the risk of simulating a different type of defect structure. At the end of the MD simulation, the structure was again optimized to minimize the potential energy before the energy of the defect structure was measured, to provide a consistent baseline and minimize thermal noise in the measurement.

In Figure 12a, we plot the average energy per point defect as determined from our MD simulations, which provides important insight into the stability of each of these types of defects. For example, the average energy of the <111> vacancy loop is greater than that of the spherical void, which means that it is energetically

favorable for large <111> vacancy loops to decompose into voids. However, we can also see that the formation energy is much more similar for small clusters, suggesting that the smaller clusters are more mobile and that vacancy loops and voids stop being distinct categories for clusters with less than 74 vacancies. This variability in the configuration of point defects is a major contributing factor to the large error in formation energies for small cluster sizes.

We can also use these calculations to obtain a model for the total formation energy of each cluster type, as shown in Figure 12b. This representation is helpful for building a mathematical model for the marginal formation energy of adding or removing a point defect from the cluster. Intuitively we know that the formation energy is primarily a function of the surface area of each type of defect. From this we can write two models to approximate the formation energy, one for a loop type defect shown in Equation 21 and another for spherical voids shown in Equation 22.

$$E_f = \nu^{2/3}\gamma n \tag{21}$$

$$E_f = 2\pi\gamma(3/4\pi\nu n)^{2/3} \tag{22}$$

where n is the number of point defects making up the cluster, gamma is the surface energy, and ν is the volume of a void or SIA. Both Equation 21 and equation 22 were found to be in excellent agreement with our simulation results for clusters larger than 100 point defects, the resulting fitted curves being able to be used in higher length scale cluster dynamics modeling. Additional work is still needed to investigate the best way to evaluate the formation energies of small clusters and how to adapt equations 21 and 22 to the small cluster sizes.

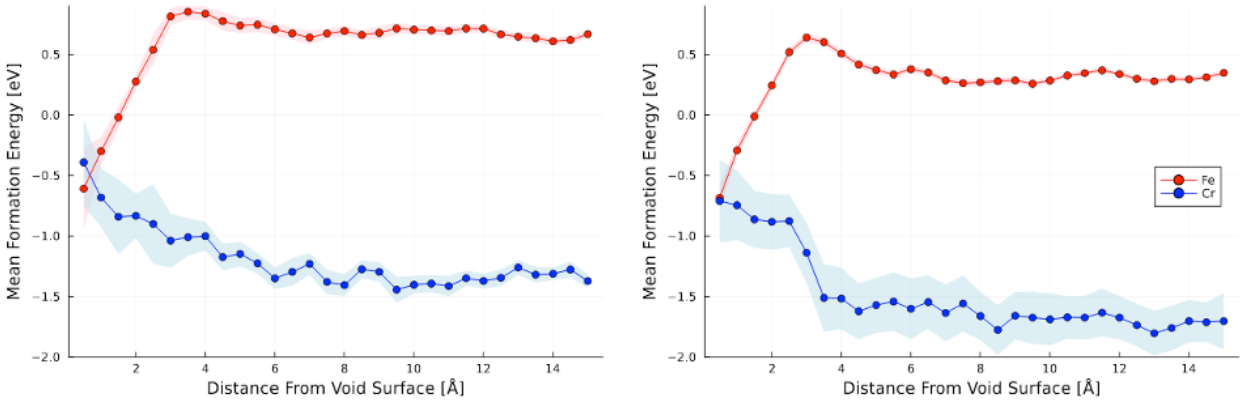

(a) (b)

Figure 13. Void formation energy in the Fe-Cr-C model as a function of distance between the location of the void and the surface of the void for voids of 8 Å (a) and 16 Å (b). The red line corresponds to the formation energy to remove an Fe atom. The blue line corresponds to the formation energy to remove a Cr atom. Shaded regions indicate one standard deviation in the measurement of the mean.

4.4. Interaction Energy Between Voids And Vacancies

Another important property for modeling the evolution of defect clusters over time is the sink strength between point defects and a given type of defect cluster. This is important because it strongly influences the rate at which defect clusters will grow and is an important set of parameters for both cluster dynamics and phase field modeling. In this current work, we have focused on the interaction between voids and vacancies to better understand the mechanisms and to build simulation techniques that can be broadly applied to understand the interaction between point defects and clusters in an alloy system like 316 stainless steel.

MD simulations were developed to measure the interaction energy between a void and vacancy separated by less than 15 Å. In order to calculate the interaction energies, a spherical void was created in our Fe-Cr-C model of 316 SS and the structure was equilibrated at 600°C. After equilibration the structure was optimized to minimize the potential energy, then a vacancy was created by randomly deleted an atom within 15 Åof the void surface, the distance from the void was recorded, the atom configuration was re-optimized. The change in potential energy was then plotted as a function of the distance from the void surface. This procedure was repeated 1000 times for each of 10 randomized atom configurations containing voids. Simulations were performed for voids with different radii.

As can be seen from the simulation results shown in 13, the potential energy to replace an Fe atom with a vacancy decreases sharply for distances under 2.5 Å. At the same time, the potential energy of removing a Cr atom rises sharply at small distances, with the change in potential energy being the same for each atom type at the surface of the void. The formation energy for Fe and Cr atoms must be the same at the surface of the void under equilibrium conditions, because the faster diffusion at the free surface allows the chemical potential of each element to equalize. An interesting detail is that this change in formation energy also suggests that the presence of a void can shift the equilibrium concentration of elements in close proximity.

The results shown here suggest that there is a strong energetic preference for Fe atoms to move into any void created by removing a Cr atom. This has important implications for understanding the capture radius of the void, since it means that the vacancy formation energy curve for Fe sites is the one which controls the diffusion of vacancies at non-zero temperatures. Previous work in the literature has found that the capture radius of a defect structure can be found by the point at which the formation energy of the vacancy is reduced by $k_b\,T$, at which point the vacancy no longer has sufficient thermal energy to escape from the void. Our simulation results indicate that this capture radius is 2.5 Å from the surface of a void for a temperature of 600° C. We also note that our results do not show the interaction energy curve having any significant dependence on the size of the void.

Additional testing was also performed using the Fe-Cr-Ni model of SS 316, shown in Figure 14. The most obvious difference is that there is no dependence on the species type of the atom removed to create the vacancy. This occurs because EAM models are isotropic and results in there being no energy barrier that prevent higher energy neighboring atoms from diffusing into a newly created vacancy at 0 K. However, we also note that even with these differences, the simulations found nearly identical results for the vacancy-void capture distance.

The capture distance calculated in this section is an important descriptor for both cluster dynamics and phase field modeling, because it is an important parameter for modeling the sink efficiency and sink strength

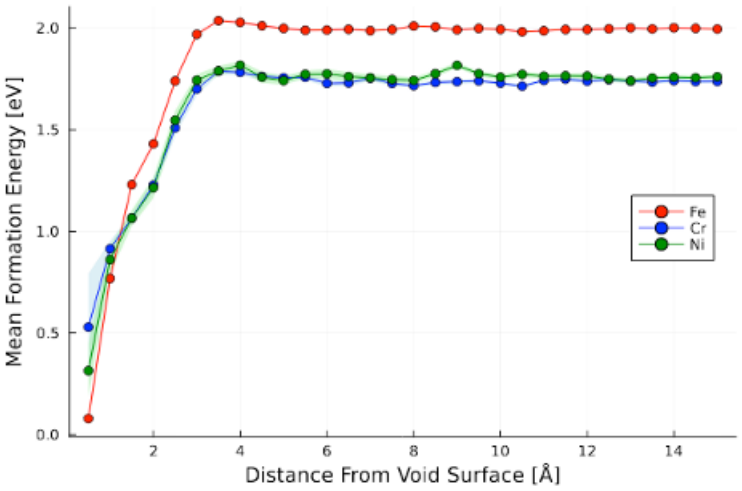

Figure 14. Void formation energy in the Fe-Cr-Ni model as a function of distance between the location of the void and the surface of the void for voids with a radius of 8 Å. Red, blue, and green lines correspond to Fe, Cr, and Ni respectively. Shaded regions indicate one standard deviation in the measurement of the mean.

of a void. The sink efficiency can be approximated as

$$Z_{i,V} = 4\pi\, r_{i,V} \tag{23}$$

where $Z_{i,V}$ is the sink efficiency of a point defect of type i interacting with a void and $r_{i,V}$ is the radius of capture measured from the center of the void to the center of the point defect [31]. This relation provides a conversion between the interaction energy data from our MD simulations and the sink efficiency parameterization that is generally used in both cluster dynamics and phase field models.

4.5. Effect Of Carbon On Vacancies And Voids

Previous experimental imaging work found that the carbon content of a sample of AM 316 stainless steel appeared to have a significant impact on the rate at which voids and other defect structures grow under irradiation. Initial atomistic modeling efforts investigated whether the carbon content had any influence on the generation of new defects during primary radiation damage [1]; however, the simulation results indicated that there was no correlation between generated point defects and carbon content in the model stainless steel system. This result indicates that carbon content at this concentration range must affect radiation-driven

Figure 15. Measurement of the total diffusion induced in a model Fe-Cr-C system due to the placement of a small vacancy cluster, with up to two carbon atoms added in close proximity.

microstructure evolution by another mechanism. Additional atomistic modeling work has been performed to determine the atomistic mechanisms by which carbon atoms may delay the evolution of cavities in 316 stainless steel.

To further our understanding of the underlying mechanisms, atomistic simulations were performed to determine the effect of carbon on the behavior of carbon atoms using the Fe-Cr-C model of 316 SS. Several different atomistic modeling techniques were attempted to verify that carbon atoms could slow the diffusion of vacancies, which could lead to slower void formation and growth. Simple diffusional simulations with varying concentrations of carbon were unable to show any difference in the diffusion rate of vacancies. However, a more direct approach of simulating mono-vacancies, di-vacancies, and tri-vacancies and then inserting one or two carbon atoms into each defect showed that carbon atoms can trap certain small vacancy clusters. This carbon-vacancy trapping is a well-studied phenomena in ferritic steels [32]. Our simulation results demonstrating the effect of carbon-vacancy trapping in the austenitic model 316 SS system are shown in Figure 15.

As can be seen in the MD simulation results, carbon trapping can be a complex phenomenon where only certain combinations of vacancies and carbon interstitials result in a reduction in the diffusion of defect clusters. It is also worth noting that in all cases tested with lone carbon atoms as well as all cases tested with mono-vacancies, no evidence of carbon-vacancy trapping was observed. This helps explain why this

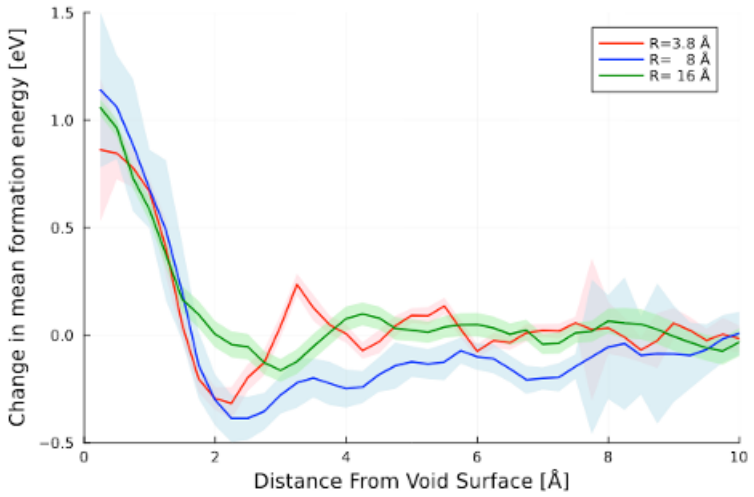

Figure 16. Comparison of the change in formation energy of carbon interstitials in the Fe-Cr system as a function of distance from the void surface. Shaded regions indicate one standard deviation from the change in the mean potential energy.

phenomenon does not occur when the carbon atoms and vacancies are randomly distributed in our general model of 316 SS.

In order to find out more about how carbon-vacancy trapping effects larger clusters of vacancies, MD simulations were developed to measure the interaction energy between a void and a carbon interstitial in an Fe-Cr alloy stabilized in the FCC phase. These simulations were performed using a similar methodology to the simulations in section 4.4, where we start with an atomic configuration containing a void equilibrated at 600° C and then measure the change in energy resulting from the insertion of a carbon interstitial at a random location within 15 Å of the void surface. Simulation results are shown in Figure 16 for Fe-Cr. Additional simulations were performed using an Fe-Cr-C alloy with 0.04 wt% C, which produced nearly identical results.

These results for the change in formation energy of the carbon interstitial show that there is a significant energy well located at approximately 2.7 Å from the surface of a void. This would suggest that carbon atoms that diffuse close to a void get trapped in a thin layer around the void. This energy well would likely result in reduced diffusion of both the void and the carbon atoms surrounding it, as it creates an additional energy barrier to diffusion. This thin layer of trapped carbon could also serve as a nucleation site for carbides. We hypothesize that this carbon trapping near the void surface is a continuation of the same phenomenon that

results in carbon trapping of small vacancy clusters; however more work is needed to verify the mechanism.

4.6. Molecular Dynamics: Discussion And Conclusions

Accurate models for predicting the formation energy of common defect structures are necessary for understanding the rate at which defect clusters grow. In order to support higher length scale simulation techniques, atomistic modeling was used to fit simple models that can be used to determine how the formation energy of common defect clusters changes as the defect grows. These models also show that large vacancy clusters are more energetically favorable than vacancy loops, but this is not as definitive for small clusters as the energy differences are less significant and the defect clusters are more easily able to rearrange themselves into different configurations.

In addition to using atomistic simulations to predict the formation energies of loops, we also developed a methodology to begin investigating the capture radii of voids through studying their interaction energy with nearby vacancies. These capture radii were found to be consistent across both the Fe-Cr-C and Fe-Cr-Ni model alloys and did not vary with the size of the void. While these energy measurements are not a direct replacement for calculating the sink strength of the void, they provide the fundamental information needed to model the recombination of point defects with voids under equilibrium conditions and provide insight into the mechanisms at play.

Motivated by experimental work that showed that the carbon content of AM 316 SS has a significant impact on the growth rate of defect clusters under irradiation, we performed several different types of MD simulation to investigate how carbon atoms interact with vacancies and voids. Atomistic simulations modeling the diffusion of small clusters of vacancies showed that the presence of carbon atoms results in the carbon-vacancy trapping that results in a significant reduction in the diffusion rate of vacancies. Additional simulations were performed to measure the interaction energy between voids and nearby carbon interstitials, which shows that there is an energy well that is capable of trapping carbon atoms near the surface of a void. Together these simulations suggest that this binding energy may be the mechanism by which the carbon

content in 316 SS slows the growth of radiation induced defects.

4.7. Density Functional Theory Introduction

The density functional theory (DFT) method is a quantum mechanics-based method that provides a first-principles approach to computing the energetic properties of crystalline materials, such as their elastic modulus, point defect energies, and defect migration barrier energies. The method finds solutions to Schrodinger's equation [33], defined as:

$$\hat{H}\Psi = E\Psi \tag{24}$$

where $\hat{H}$ is the Hamiltonian that operates on Ψ, Ψ is the wave function, and E is the energy of the system. DFT arises from application of the Born-Oppenheimer approximation, which assumes that the electronic and nuclear wave functions can be treated separately due to the mass difference between electrons and nuclei [34]. Kohn and Sham [35] developed equations based on the time-independent Schrodinger equation [33], which allow DFT to be a viable computational method for modeling materials. Because the equations developed by Kohn and Sham are time-independent and the energetic ground state occurs at 0 K by definition, DFT calculations deal with static systems at 0 K.

All quantum mechanical properties are calculated using DFT in the Vienna Ab-initio Simulation Package (VASP) [36, 37] within the periodic boundary condition approach. The Perdew-Burke-Ernzerhof form of the generalized gradient approximation exchange-correlation functional [38] with the projector augmented wave pseudopotentials [39] are employed. No Hubbard correction is used due to the metallic nature of the systems investigated. Spin-polarized calculations were applied, and spins were allowed to relax. DFT calculations use a summation of plane waves with energies up to 600 eV for 316 SS. Increasing the cutoff value to 650 eV alter system energies by only 7.6×10^{-3} eV. A gamma point centered k-point mesh of $4 \times 4 \times 4$ are chosen for the 316 SS system because increasing this mesh to $6 \times 6 \times 6$ only alters the system energy by 8.8×10^{-3} eV. First order Methfessel-Paxton smearing of the bands are applied with a width of 0.10 eV. The electronic convergence criterion is set to 1.0×10^{-5} eV for all DFT calculations. Geometries are optimized until they

converge to energy changes of less than 1.0×10^{-4} eV. We note that the vacancy concentration in 316 SS is very high (1.4 at. %) in these simulations. However, when the system is extended in one direction (from a $1 \times 1 \times 1$ to a $2 \times 1 \times 1$), the vacancy formation energy only changes by 7.0×10^{-3} eV (0.23 %). Thus, we consider our vacancy concentration value reasonable for the prediction of vacancy migration energy barriers (E_v^b).

The stochastic nature of the solid solution 316 SS material is accounted for through application of special quasirandom structures [40]. This is accomplished by generating a large number of structures and comparing the radial distribution functions of each until a sufficiently close match to the targeted random substitution is found. Our special quasirandom structures generated 316 SS results in an mean average error of 1.2×10^{-3} (arbitrary units) or 1.1 %. The 316 SS composition in this work omits minor elements and uses a composition of 66 at. % Fe, 22 at. % Cr, and 11 at. % Ni; although this is an excess of Cr versus the 316 SS specification, this composition was the closest achievable within the constraints of the special quasirandom structures method and number of atoms within the simulation.

4.8. Machine-Learned Nudged Elastic Band Introduction

The machine-learned nudged elastic band (ML-NEB) method builds upon the well-established nudged elastic band (NEB) method to learn the potential energy surface (PES) of a given material and migration energy barrier of a given reaction. The NEB method finds the saddle point and minimum energy path between a reactant-product pair. This is accomplished by relaxing a series of interpolated atomic configurations, known as images, along the reaction pathway while maintaining equal space between each image. This spacing is maintained through spring forces applied along the band. These spring forces also project a force component against the slope of the PES perpendicular to the band so that the band is nudged towards the saddle point (or transition state) of the PES between the reactant and product [41].

The ML-NEB method extends the NEB method by application of Gaussian process regression (GPR). GPR can infer continuous variables, such as energy values on a potential energy surface, by first defining

an initial distribution of values to be a Gaussian process [42, 43] (a collection of random values such that any finite subset has a multivariate normal distribution). Applying Bayesian inference, this initial Gaussian process is updated based on observations of data [44, 45]. In ML-NEB, images are generated as in the NEB method, but they are initially relaxed electronically (i.e., only the electron density is evolved) instead of ionically (i.e., the positions of the atomic nuclei are allowed to move in addition to the electron density). The potential energy surface is modeled by GPR, being initialized by a Gaussian process and updated by Bayesian inference. Because the distributions used to model the potential energy surface are Gaussian, calculated force uncertainties are readily available. These uncertainties are used to determine if the more computationally expensive ionic relaxation is required, according to a predetermined convergence criteria. Thus, computational cost is decreased by minimizing the number of computationally expensive ionic relaxations and replacing them with more computationally efficient electronic relaxations. This process continues until the convergence criteria, usually calculated force uncertainty, is met [46, 47]. 316 SS ML-NEB calculations converged in under 48 hours; however, traditional NEB calculations did not converge within a month, prohibiting comparison. We therefore benchmarked the ML-NEB method against traditional NEB using FCC Fe as a surrogate system for 316 SS and found that ML-NEB completed 2.3 times faster and differed from NEB calculated E_v^m by only 2.7×10^{-2} eV (1.0 %).

4.9. Modified Gaussian Process Regression Introduction

The ML-NEB predicted E_v^b are used to train a Gaussian process external to the ML-NEB method to analyze E_v^b in the compositional space local to vacancies in 316 SS. This is accomplished through the scikit-learn python package [48], and uses several compositions to construct the descriptor array. First, the composition of the first, second, and third nearest neighbors (NN) of the initial and final vacancy hop sites are collected. Next, the site intersections of the first and third NN between the initial and final vacancy hop sites are included, so as to describe the composition near the transition state. Finally, the atomic number (Z) of the element diffusing opposite the vacancy is added. The Gaussian process is then used to predict

E_v^b, but is modified to improve error as follows: if the uncertainty is above a specific value (in this case, 1.0×10^{-5} eV), the code will again predict E_v^b using only the E_v^b from ML-NEB and associated descriptor arrays that have the same composition values for the transition state and same element diffusing opposite the vacancy as the descriptor array being used to predict E_v^b. Then the uncertainty is compared again; if still above the specific value, the Gaussian process is used to predict E_v^b using only those E_v^b from ML-NEB and associated descriptor arrays that have the same composition values for only the first NN of the transition state and same element diffusing opposite the vacancy as the descriptor array being used to predict E_v^b. Finally, if the uncertainty is still too large, the Gaussian process is used to predict E_v^b using only those ML-NEB E_v^b and associated descriptor arrays that have the same Z for the element diffusing opposite the vacancy as the descriptor array being used to predict E_v^b. We term this process modified Gaussian process regression (MGPR).

For comparison to our MGPR predicted E_v^b, we calculate E_v^b using four MD embedded atom method (EAM) potentials [29, 49–51]. We note that the compositional space local to the vacancy (as described by the descriptor array) is the same between ML-NEB and MGPR predicted E_v^b values, but is not in the MD EAM E_v^b cases. As such, these methods are only compared by E_v^b averages by element diffusing opposite the vacancy. E_v^b averages for Cr, Fe, and Ni diffusing opposite the vacancy for ML-NEB and MGPR are over 32, 138, and 30 E_v^b values, respectively. MD EAM E_v^b averages for Cr, Fe, and Ni are over 50 E_v^b values each.

4.10. Kinetic Monte Carlo Introduction

The kinetic Monte Carlo (KMC) method allows for the extension of DFT results to time-based processes (e. g., diffusion) as well as the inclusion of finite temperature. This is accomplished by computing many iterations of a possible event over randomly selected points in a lattice, with each iteration determining if an action (e.g., a vacancy hop) will occur based on some acceptance criterion (e.g., a Boltzmann distribution) [52]. Our KMC model employs a Boltzmann distribution to determine vacancy hops and uses only a small preliminary system: a 4×4×4 supercell (256 atoms) of roughly 66 at. % Fe, 22 at. % Cr, and 11 at. % Ni and

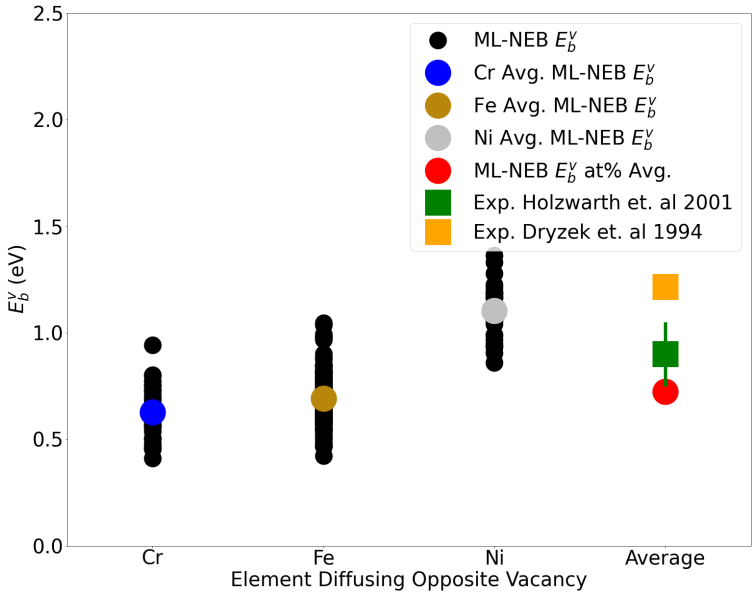

Figure 17. ML-NEB calculated E_v^b averaged by element diffusing opposite the vacancy. Far right plots overall average ML-NEB E_v^b as compared to experimental E_v^b from positron annihilation spectroscopy.

a total of 3.1×10^6 vacancy hops. We selected 1200 K for our initial KMC simulation runs, and account for vacancy concentration at this temperature by using the mean of an experimentally derived value which is similar to others quenched at 1323 K [53].

4.11. Local Compositional Dependence Of Vacancy Migration Energy Barriers

ML-NEB predicted vacancy migration energy barriers (E_v^b) show qualitative agreement with experiment [5]. Figure 17 plots the E_v^b averaged by element diffusing opposite the vacancy, showing Cr has the lowest E_v^b, followed closely by Fe, while Ni is over 1.5 times that of Fe. Einstein's equation [54] shows that these E_v^b values are exponentially inversely proportional to diffusivity, which when applied, predicts Cr to diffuse fastest, followed by Fe, then Ni. This is what Yang et. al [5] shows, with Cr diffusivity being 1.61 times that of Fe and 2.35 times that of Ni at 593 K. With this validation, we proceed to accelerate the prediction of these E_v^b values by through a modified Gaussian process regression (MGPR) applied to the ML-NEB E_v^b results.

Our MGPR allows for more rapid and accurate E_v^b prediction than four different molecular dynamics embedded atom method (MD EAM) potentials [29, 49–51]. Figure 18 plots the E_v^b averaged by element

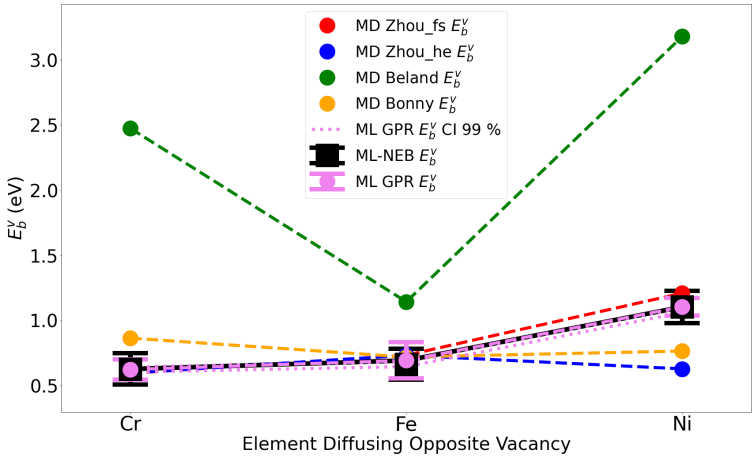

Figure 18. ML-NEB, GPR, and MD predicted E_v^b averaged by element diffusing opposite the vacancy. A 99 % confidence interval is plotted for the GPR results.

diffusing opposite the vacancy as predicted by ML-NEB, MGPR (trained and tested on 80 and 20 % of the ML-NEB data, respectively), and four MD EAM potentials, showing the MGPR E_v^b values to be closest to ML-NEB E_v^b values. Only MGPR and Zhou_fs [50] show the same E_v^b trend with respect to element diffusing opposite the vacancy, which makes Zhou_fs appear to approximate the accuracy of MGPR. However, the average E_v^b as predicted by Zhou_fs for Ni diffusing opposite the vacancy includes an outlying E_v^b value of 7.98 eV. If this outlier, and others like it, are removed, then only the MGPR E_v^b trend with elements diffusing opposite the vacancy in agreement with ML-NEB E_v^b. In addition to its accuracy, the MGPR method is at least 500 times as fast as any of the MD EAM potentials for this computational task. Having confirmed the accuracy and efficiency of MGPR, we apply MGPR to understand the effects of local composition on E_v^b in 316 SS.

According to the results of our MGPR study, the we find that the greatest effect on E_v^b in 316 SS is the Ni content of the first NN shell of the vacancy. Figure 19 plots all the compositionally unique MGPR-predicted E_v^b in a 10x10x10 $Fe_{0.67}Cr_{0.22}Ni_{0.11}$ supercell (4000 atoms) as a function of the Ni at. % of the initial vacancy site's first NN shell. We determine which position (initial, transition, or final), NN group (first, second, or third), and which element composition (Cr, Fe, Ni) has the most impact on E_v^b by computing the magnitude of a simple linear fit to each of these cases as well as the coefficient of determination (R^2). The Ni content of

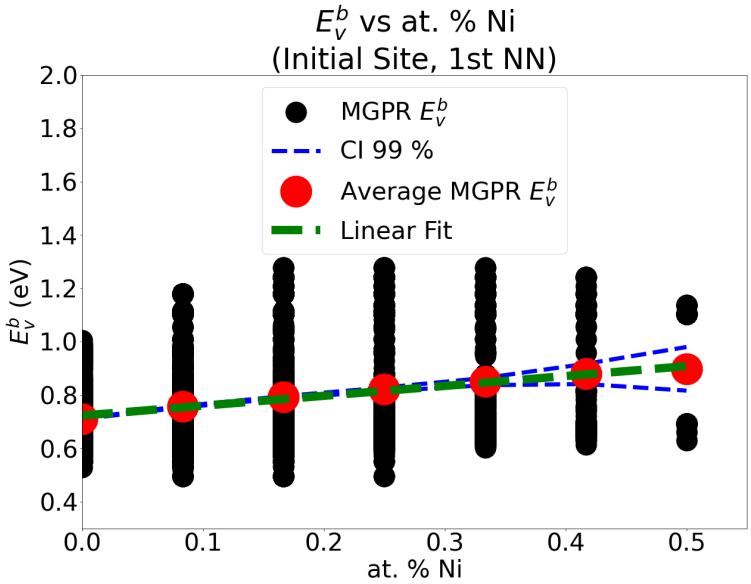

Figure 19. The MGPR E_v^b are plotted as a function of Ni at. % of the first NN shell around the initial vacancy site in a 10×10×10 supercell (4000 atoms). The MGPR E_v^b values and at. % Ni average MGPR E_v^b are represented by black and red circles, respectively. The 99 % confidence interval range and linear fit line are represented by blue and green dashed lines, respectively.

the vacancy's first NN shell in the initial vacancy position has the highest R^2 value and slope magnitude (0.99 and 0.37 eV, respectively) of all 28 cases (excepting the dependence of which element is diffusing opposite the vacancy, as this has already been demonstrated by our work and previous experiment [5]). The next highest R^2 values and slope magnitudes are found in the initial vacancy position in the first NN shell for Fe (0.84 and -0.16 eV, respectively) and Cr (0.76 and -0.15 eV). The high R^2 values and negative slopes associated with Fe and Cr content imply that E_v^b may be increased by Ni substitution of Fe and Cr in the initial vacancy position, first NN shell. According to these results, increasing the Ni content of the vacancy's first NN shell from 0 to 42 at% is proportional to a reduction in the vacancy hop probability by a factor of between 4 and 11 at 1000 K. We therefore hypothesize that increasing the Ni content in 316 SS (or more generally, the entire class of austenitic Fe-Ni-Cr alloys) could lead to an decrease in vacancy diffusivity in the material. This should be especially true if Ni content replaces Cr content, as experimental work [5] and this work show Cr to have the highest diffusivity opposite the vacancy. With trends in E_v^b as a function of local composition elucidated, we employ KMC simulations to understand vacancy diffusivity.

4.12. Local Compositional Dependence Of Vacancy Diffusivity

Preliminary KMC results show qualitative agreement with tracer experiments by Yang et. al [5], with Cr diffusing fastest opposite the vacancy, followed by Fe, then Ni. Our KMC-calculated diffusivity coefficients (D_0) are 3.0×10^{-13}, 4.7×10^{-14}, and 9.6×10^{-16} m^2/s, for Cr, Fe, and Ni, respectively. Quantitatively, these results do not show good agreement; our Cr partial diffusivity value is off by a factor of approximately 10 relative to Cr partial diffusivity calculated by Yang et. al [5] and even the ratios of the diffusivities are in disagreement (by a factor of ~100 in the case of the Cr-Ni D_0 ratio). This disparity is shown in Table 3, both between Yang et. al and two other experimental works [55, 56]. We attribute the Cr diffusivity discrepancies to differences in composition between our work and Yang et. al. The large ratio discrepancies are attributed to insufficient number of vacancy hops in the case of Ni. Specifically, Cr and Fe atoms hop opposite the vacancy over 8.0×10^5 times, while Ni does so less than 4.0×10^3 in the KMC simulations (due to the high Ni E_v^b values). Thus, while these preliminary KMC diffusivity results show qualitative agreement with experimental trend, more must be done to completely describe Fe and Ni diffusion opposite the vacancy in 316 SS.

Table 3. Comparison of D_0 ratios of elements diffusing opposite vacancies.

Author	**at. % Cr**	**at. % Ni**	D_{0Cr}/D_{0Fe}	D_{0Cr}/D_{0Ni}
Yang et. al [5]	15	20	1.73 $\pm$0.04	2.57 $\pm$0.04
Rothman et. al [55]	15	20	1.67 $\pm$0.31	2.55 $\pm$0.57
Jönsson et. al [56]	15	20	1.06 $\pm$0.09	1.87 $\pm$0.02
current work	22	11	6.3	3.1×10^2

4.13. Vacancy Migration Barriers: Conclusions

The combination of ML-NEB and our MGPR suggest that increasing Ni content in 316 SS (or by extension, the general austenitic Fe-Cr-Ni alloy system) may slow vacancy diffusion in this nuclear structural material. This could provide a mechanism for the observed reduction in transient swelling rate for austenitic Fe-Cr-Ni alloys with increasing Ni content [57]. Beyond the ternary 316 SS system analyzed here, this methodology

can be extended to any system for which vacancy diffusivity and its dependence on local composition are of interest. This includes other potential nuclear structural alloys, such as high entropy alloys, for which irradiation resistance by slowing vacancy diffusion is important.

5. CONCLUSIONS

This milestone presents multi-scale modeling research results for additively manufactured 316 stainless steel. We use a combination of phase field, cluster dynamics, molecular dynamics, and density functional theory with machine learning. This combined modeling approach allows for predictions of radiation-driven microstructural evolution in LPBF 316 SS over a range of temperatures, dpa damage rates, neutron spectra, and microstructures, and supports the development of the use of combined ion and neutron irradiation for materials qualification. Informed by ion irradiation and neutron irradiation results across the AMMT program, we develop physics-based and machine learning models for the unique aspects of radiation-driven microstructure evolution in LPBF 316. In particular, we focus on understanding the impact of carbon concentration (varying, for example, between the 316L and 316H standards) on void formation; radiation-induced segregation at dislocation cells and grain boundaries; and the evolution of dislocation loops and network dislocation populations.

The development of mean-field models integrated with spatially-dependent AM microstructures and rate-theory RIS within the MOOSE framework has advanced the understanding of line dislocation evolution. These models consider the complexities of the AM microstructures and have shown that pipe diffusion plays a significant role in dislocation evolution and RIS at low temperatures. We compared two models for the thermal recovery of dislocations, which is a necessary aspect of modeling radiation damage behavior at the relatively high temperatures of advanced reactor applications. We found that the unique characteristics of the AM microstructures must be captured in a thermal recovery model to accurately model the dislocation evolution. In addition, in describing the dislocation climb velocity, the variation in sink strengths (or bias variance) arising due to the variation in dislocation density was found to be important. Simulations of the

spatially-resolved model demonstrated the decrease in cell wall dislocation density, the generation of new bulk dislocations, and the overall disappearance of the cell structure, similar to what is observed experimentally with ion and neutron irradiation. Finally, good quantitative agreement for RIS is found between models and experiments. Cr depletion and Ni enrichment was observed at the cell walls and grain boundaries, with the magnitudes being lower at the cell walls. Moreover, the relative extents of Cr and Ni RIS were found to be different at the cell walls due to their biased sink behavior.

We have also implemented mean-field cluster dynamics model from literature that can be effectively used to predict the evolution of irradiation defects in additively manufactured 316 stainless steel, which is a crucial capability in being able to combine ion and neutron irradiation testing for accelerated material qualification. In the current model, the irradiation defects considered are the SIA and vacancy dislocation loops, based on the work by Pokor et al. [20]. The predicted evolution of the loop population shows growth and coarsening of large SIA loops and an accumulation of small vacancy loops without any significant growth due to the sluggish kinetics of vacancies, which restricts their diffusion and migration to loops and sinks, even at high temperature and irradiation dose rates. Significantly, the CD model predictions of loop growth versus temperature at a given damage rate have good qualitative agreement with ion irradiation results from within the AMMT program (i.e., rapid onset of loop formation at 350°C, while loop formation is suppressed until higher damage levels at 650°C). In addition, the CD model sheds light on the effect of dislocation sinks on the evolution of loops. SIA loop growth is suppressed at a high dislocation sink density, promoting an almost two order of magnitude increase in the number of small vacancy loops in the matrix. A similar observation is also expected for the presence of voids in AM 316. Concurrent evolution of network dislocation sinks, with SIA and vacancy loops, will be included in the CD model in the next phase of research, which will allow us to study the evolution of dislocation sink density with a climb-glide mechanism due to the migration of SIA and vacancies generated in the displacement cascade.

At the atomistic scale, machine learning combined with density functional theory was used to study the vacancy migration energies of the ternary Fe-Cr-Ni system within the range of 316 SS composition. The

results suggest that increasing Ni content can slow vacancy diffusion, which may provide a mechanism for the observed reduction in transient swelling rate for austenitic Fe-Cr-Ni alloys with increasing Ni content [57]. In addition, ion irradiations have shown that increasing carbon content in 316 SS results in a larger population of smaller voids, suggesting reduced vacancy diffusion. MD simulations have shown that the carbon content of AM 316 SS has a significant impact on the migration rate of defect clusters. The presence of carbon atoms results in carbon-vacancy trapping, significantly reducing the diffusion rate of vacancies. MD results also found that carbon atoms may be trapped near the surface of a void, which may reduce void growth by trapping vacancies that diffuse toward the void.

In order to support higher length scale simulation techniques, atomistic modeling was used to fit simple models that can be used to determine how the formation energy of common defect clusters changes as the defect grows. These models also show that large vacancy clusters are more energetically favorable than vacancy loops, and that the energy of different cluster configurations converges with decreasing size because the defect clusters are more easily able to rearrange themselves into different configurations. We also developed a methodology to investigate the defect capture radii of voids through studying their interaction energy with nearby vacancies. These capture radii were found to be consistent across both the Fe-Cr-C and Fe-Cr-Ni model alloys and did not vary with the size of the void. While these energy measurements are not a direct replacement for calculating the sink strength of the void, they provide the fundamental information needed to model the recombination of point defects with voids under equilibrium conditions.

[1] A. M. Jokisaari, P. Baldo, W. Chen, Y. Chen, D. Harbaruk, S. B. Kadambi, J.-H. Ke, M. M. Swisher, and J. Hlavenka, "Preliminary results addressing material qualification using combined ion irradiation and modeling data," Tech. Rep. INL/RPT-23-74848-Rev000, Idaho National Laboratory (INL), Idaho Falls, ID (United States), 2023.

[2] A. A. Kohnert and L. Capolungo, "The kinetics of static recovery by dislocation climb," *npj Computational Materials*, vol. 8, no. 1, p. 104, 2022.

[3] W. Wolfer and B. Glasgow, "Dislocation evolution in metals during irradiation," *Acta Metallurgica*, vol. 33, no. 11, pp. 1997–2004, 1985.

[4] T. Jourdan, "Influence of dislocation and dislocation loop biases on microstructures simulated by rate equation cluster dynamics," *Journal of Nuclear Materials*, vol. 467, pp. 286–301, 2015.

[5] Y. Yang, K. G. Field, T. R. Allen, and J. T. Busby, "Roles of vacancy/interstitial diffusion and segregation in the microchemistry at grain boundaries of irradiated Fe–Cr–Ni alloys," *Journal of Nuclear Materials*, vol. 473, pp. 35–53, 2016.

[6] G. S. Was, *Fundamentals of radiation materials science : Metals and alloys*. New York: Springer, second edition ed., 2017.

[7] T. Allen and G. Was, "Modeling radiation-induced segregation in austenitic Fe–Cr–Ni alloys," *Acta Materialia*, vol. 46, no. 10, pp. 3679–3691, 1998.

[8] J. R. Manning, "Correlation factors for diffusion in nondilute alloys," *Physical Review B*, vol. 4, no. 4, p. 1111, 1971.

[9] M. J. Hackett, J. T. Busby, and G. Was, "The mechanism of Zr and Hf in reducing radiation-induced

segregation in 316 stainless steel," *Metallurgical and Materials Transactions A*, vol. 39, pp. 218–224, 2008.

[10] C. J. Permann, M. R. Tonks, B. Fromm, and D. R. Gaston, "Order parameter re-mapping algorithm for 3D phase field model of grain growth using FEM," *Computational Materials Science*, vol. 115, pp. 18–25, 2016.

[11] P.-C. Simon, L. K. Aagesen, C. Jiang, W. Jiang, and J.-H. Ke, "Mechanistic calculation of the effective silver diffusion coefficient in polycrystalline silicon carbide: Application to silver release in AGR-1 TRISO particles," *Journal of Nuclear Materials*, vol. 563, p. 153669, 2022.

[12] K. Bertsch, G. Meric de Bellefon, B. Kuehl, and D. Thoma, "Origin of dislocation structures in an additively manufactured austenitic stainless steel 316l," *Acta Materialia*, vol. 199, pp. 19–33, 2020.

[13] G. Meric de Bellefon, K. Bertsch, M. Chancey, Y. Wang, and D. Thoma, "Influence of solidification structures on radiation-induced swelling in an additively-manufactured austenitic stainless steel," *Journal of Nuclear Materials*, vol. 523, pp. 291–298, 2019.

[14] Z. Shang, C. Fan, S. Xue, J. Ding, J. Li, T. Voisin, Y. M. Wang, H. Wang, and X. Zhang, "Response of solidification cellular structures in additively manufactured 316 stainless steel to heavy ion irradiation: an in situ study," *Materials Research Letters*, vol. 7, no. 7, pp. 290–297, 2019.

[15] L. Jiang, M. Song, L. Yang, J. Yang, D. Du, X. Lou, and Y. Chen, "A comparison study of void swelling in additively manufactured and cold-worked 316L stainless steels under ion irradiation," *Journal of Nuclear Materials*, vol. 551, p. 152946, 2021.

[16] S. Li, J. Hu, W.-Y. Chen, J. Yu, M. Li, and Y. Wang, "Evolution of cellular dislocation structures and defects in additively manufactured austenitic stainless steel under ion irradiation," *Scripta Materialia*, vol. 178, pp. 245–250, 2020.

[17] A. A. Kohnert, B. D. Wirth, and L. Capolungo, "Modeling microstructural evolution in irradiated materials with cluster dynamics methods: A review," *Computational Materials Science*, vol. 149, pp. 442–459, 2018.

[18] N. M. Ghoniem, "Clustering theory of atomic defects," *Radiation Effects and Defects in Solids*, vol. 148, no. 1-4, pp. 269–318, 1999.

[19] A. Hardouin Duparc, C. Moingeon, N. S. de Grande, and A. Barbu, "Microstructure modelling of ferritic alloys under high flux 1 MeV electron irradiations," *Journal of Nuclear Materials*, vol. 302, no. 2, pp. 143–155, 2002.

[20] C. Pokor, Y. Brechet, P. Dubuisson, J.-P. Massoud, and A. Barbu, "Irradiation damage in 304 and 316 stainless steels: experimental investigation and modeling. Part I: Evolution of the microstructure," *Journal of Nuclear Materials*, vol. 326, no. 1, pp. 19–29, 2004.

[21] A. D. Brailsford and R. Bullough, "The theory of sink strengths," *Philosophical Transactions of the Royal Society of London. Series A, Mathematical and Physical Sciences*, vol. 302, pp. 87–137, 1981.

[22] M. Kiritani, "Analysis of the clustering process of supersaturated lattice vacancies," *Journal of the Physical Society of Japan*, vol. 35, no. 1, pp. 95–107, 1973.

[23] A. V. B. S. I. Golubov, A. M. Ovcharenko and B. N. Singh, "Grouping method for the approximate solution of a kinetic equation describing the evolution of point-defect clusters," *Philosophical Magazine A*, vol. 81, no. 3, pp. 643–658, 2001.

[24] A. A. Kohnert and B. D. Wirth, "Grouping techniques for large-scale cluster dynamics simulations of reaction diffusion processes," *Modelling and Simulation in Materials Science and Engineering*, vol. 25, p. 015008, dec 2016.

[25] A. P. Thompson, H. M. Aktulga, R. Berger, D. S. Bolintineanu, W. M. Brown, P. S. Crozier, P. J. in 't Veld, A. Kohlmeyer, S. G. Moore, T. D. Nguyen, R. Shan, M. J. Stevens, J. Tranchida, C. Trott, and S. J.

Plimpton, “LAMMPS - a flexible simulation tool for particle-based materials modeling at the atomic, meso, and continuum scales,” *Computer Physics Communications*, vol. 271, p. 108171, 2022.

[26] J. Tersoff, “New empirical approach for the structure and energy of covalent systems,” *Physical Review B*, vol. 37, pp. 6991–7000, Apr 1988.

[27] K. O. E. Henriksson, C. Björkas, and K. Nordlund, “Atomistic simulations of stainless steels: a many-body potential for the Fe–Cr–C system,” *Journal of Physics: Condensed Matter*, vol. 25, no. 44, p. 445401, 2013.

[28] M. S. Daw and M. I. Baskes, “Embedded-atom method: Derivation and application to impurities, surfaces, and other defects in metals,” *Physical Review B*, vol. 29, pp. 6443–6453, Jun 1984.

[29] G. Bonny, N. Castin, and D. Terentyev, “Interatomic potential for studying ageing under irradiation in stainless steels: the fenicr model alloy,” *Modelling and Simulation in Materials Science and Engineering*, vol. 21, p. 085004, oct 2013.

[30] P. Hirel, “Atomsk: A tool for manipulating and converting atomic data files,” *Computer Physics Communications*, vol. 197, pp. 212–219, 2015.

[31] A. A. Kohnert, M. A. Cusentino, and B. D. Wirth, “Molecular statics calculations of the biases and point defect capture volumes of small cavities,” *Journal of Nuclear Materials*, vol. 499, pp. 480–489, 2018.

[32] T. Kresse, C. Borchers, and R. Kirchheim, “Vacancy–carbon complexes in bcc iron: Correlation between carbon content, vacancy concentration and diffusion coefficient,” *Scripta Materialia*, vol. 69, no. 9, pp. 690–693, 2013.

[33] E. Schrödinger, “An undulatory theory of the mechanics of atoms and molecules,” *Physical Review*, vol. 28, no. 6, p. 1049, 1926.

[34] N. W. Ashcroft and N. D. Mermin, *Solid state physics*. Cengage Learning, 1976.

[35] W. Kohn and L. J. Sham, "Self-consistent equations including exchange and correlation effects," *Physical Review*, vol. 140, no. 4A, p. A1133, 1965.

[36] G. Kresse and J. Furthmüller, "Efficient iterative schemes for ab initio total-energy calculations using a plane-wave basis set," *Physical Review B*, vol. 54, no. 16, p. 11169, 1996.

[37] G. Kresse and J. Furthmüller, "Efficiency of ab-initio total energy calculations for metals and semiconductors using a plane-wave basis set," *Computational Materials Science*, vol. 6, no. 1, pp. 15–50, 1996.

[38] J. P. Perdew, K. Burke, and M. Ernzerhof, "Generalized gradient approximation made simple," *Physical Review Letters*, vol. 77, no. 18, p. 3865, 1996.

[39] G. Kresse and D. Joubert, "From ultrasoft pseudopotentials to the projector augmented-wave method," *Physical Review B*, vol. 59, no. 3, p. 1758, 1999.

[40] A. Zunger, S.-H. Wei, L. Ferreira, and J. E. Bernard, "Special quasirandom structures," *Physical Review Letters*, vol. 65, no. 3, p. 353, 1990.

[41] H. Jónsson, G. Mills, and K. W. Jacobsen, "Nudged elastic band method for finding minimum energy paths of transitions," in *Classical and quantum dynamics in condensed phase simulations*, pp. 385–404, World Scientific, 1998.

[42] C. E. Rasmussen, C. K. Williams, *et al.*, *Gaussian processes for machine learning*, vol. 1. Springer, 2006.

[43] W. Liu, J. C. Principe, and S. Haykin, *Kernel adaptive filtering: a comprehensive introduction*. John Wiley & Sons, 2011.

[44] M. Taboga, ""Bayesian inference", Lectures on probability theory and mathematical statistics," 2021.

[45] J. M. Bernardo and A. F. Smith, *Bayesian theory*, vol. 405. John Wiley & Sons, 2009.

[46] M. H. Hansen, J. A. G. Torres, P. C. Jennings, Z. Wang, J. R. Boes, O. G. Mamun, and T. Bligaard, "An atomistic machine learning package for surface science and catalysis," *arXiv preprint arXiv:1904.00904*, 2019.

[47] J. A. G. Torres, P. C. Jennings, M. H. Hansen, J. R. Boes, and T. Bligaard, "Low-scaling algorithm for nudged elastic band calculations using a surrogate machine learning model," *Physical Review Letters*, vol. 122, no. 15, p. 156001, 2019.

[48] F. Pedregosa, G. Varoquaux, A. Gramfort, V. Michel, B. Thirion, O. Grisel, M. Blondel, P. Prettenhofer, R. Weiss, V. Dubourg, J. Vanderplas, A. Passos, D. Cournapeau, M. Brucher, M. Perrot, and E. Duchesnay, "Scikit-learn: Machine learning in Python," *Journal of Machine Learning Research*, vol. 12, pp. 2825–2830, 2011.

[49] L. K. Béland, A. Tamm, S. Mu, G. Samolyuk, Y. Osetsky, A. Aabloo, M. Klintenberg, A. Caro, and R. Stoller, "Accurate classical short-range forces for the study of collision cascades in Fe–Ni–Cr," *Computer Physics Communications*, vol. 219, pp. 11–19, 2017.

[50] X. W. Zhou, M. E. Foster, and R. B. Sills, "An Fe-Ni-Cr embedded atom method potential for austenitic and ferritic systems," *Journal of Computational Chemistry*, vol. 39, no. 29, pp. 2420–2431, 2018.

[51] X. Zhou, M. Foster, and R. Sills, "Enabling molecular dynamics simulations of helium bubble formation in tritium-containing austenitic stainless steels: An Fe-Ni-Cr-H-He potential," *Journal of Nuclear Materials*, vol. 575, p. 154232, 2023.

[52] M. Andersen, C. Panosetti, and K. Reuter, "A practical guide to surface kinetic Monte Carlo simulations," *Frontiers in chemistry*, vol. 7, p. 202, 2019.

[53] J. Dryzek, C. Wesseling, E. Dryzek, and B. Cleff, "Migration of vacancies in stainless steel measured by positron annihilation," *Materials Letters*, vol. 21, no. 2, pp. 209–214, 1994.

[54] A. Einstein, “Über die von der molekularkinetischen theorie der wärme geforderte bewegung von in ruhenden flüssigkeiten suspendierten teilchen,” *Annalen der physik*, vol. 4, 1905.

[55] S. Rothman, L. Nowicki, and G. Murch, “Self-diffusion in austenitic Fe-Cr-Ni alloys,” *Journal of Physics F: Metal Physics*, vol. 10, no. 3, p. 383, 1980.

[56] B. Jönsson, “Assessment of the mobility of carbon in fcc C-Cr-Fe-Ni alloys,” *International Journal of Materials Research*, vol. 85, no. 7, pp. 502–509, 1994.

[57] F. A. Garner and H. R. Brager, “Swelling of austenitic iron-nickel-chromium ternary alloys during fast neutron irradiation,” in *Effects of Radiation on Materials: Twelfth International Symposium, ASTM STP*, vol. 870, pp. 187–201, 1985.